A nonhydrostatic oceanic regional model ORCTM v1 for internal solitary wave simulation

Hao Huang[1], Pengyang Song[1,2], Shi Qiu[1], Jiaqi Guo[1], Xueen Chen[1]

[1]Frontier Science Center for Deep Ocean Multispheres and Earth System (FDOMES) and Physical Oceanography Laboratory, Ocean University of China, Qingdao, 266100, China

[2]Alfred Wegener Institute for Polar and Marine Research, Bremerhaven, Germany

Correspondence to: Xueen Chen (xchen@ouc.edu.cn)

Abstract.

An Oceanic Regional Circulation and Tide Model (ORCTM) including the nonhydrostatic dynamics module which can numerically reproduce the Internal Solitary Waves (ISWs) dynamics, is presented in this paper. The performance of baroclinic tidal simulation is also examined in the regional modelling with the open boundary conditions.

The model control equations are characterized with the three-dimensional and fully nonlinear forms considering incompressible Boussinesq fluid in Z-coordinates. The pressure field is decomposed into the surface, hydrostatic, and nonhydrostatic components on the orthogonal curvilinear Arakawa-C grid. The nonhydrostatic pressure determined by the intermediate velocity divergence field is obtained via solving a three-dimensional Poisson equation based on a pressure correction method. Model validation experiments for ISWs simulations with the topographic change in the two-layer and continuously stratified ocean demonstrate that ORCTM has a considerable capacity for reproducing the life cycle of Internal Solitary Waves evolution and tide-topography interactions.

1. Introduction

Internal Waves (also called Internal Gravity Waves) activities have been observed frequently across the stratified ocean and play a significant role in the multiscale energy cascade (Mtfller, 1976). Observations reveal that the Internal Waves, especially the high-frequency Internal Solitary Waves, could contain significant potential energy with strong vertical shear, mixing, and wave breaking, leading to a dramatic change of the currents and density structures (Ramp et al., 2004; Vlasenko et al., 2010; Huang et al., 2016), violent overturning bringing sediment and nutrient from the seafloor to the surface (Wang et al., 2007), even irretrievable damages to some underwater vehicles (Duda et al., 2006) and deep-water

29   drilling (Osborne et al., 1978). Basically, astronomical tides passing the abrupt topography can cause the

30   generation of baroclinic tides (also called internal tides, hereafter ITs) with multi-modal structures then

31   capable of propagation, disintegration, and dissipation in the ocean (Vlasenko et al., 2005; 2010). The

32   low-mode of baroclinic tides can travel thousands of kilometers with long horizontal wavelengths about

33   ten of kilometers (Baines, 1982). Furthermore, the inclusion of nonlinear and nonhydrostatic effects

34   permits the evolution of the Nonlinear Internal Waves (hereafter NIWs), even the Internal Solitary Waves

35   (hereafter ISWs) derived from the steepening of low-mode internal tides as the consequence of the ever-

36   changing terrain and background stratification (Gerkema and Zimmerman, 1995; legg and Adroft, 2003).

37   Numerical ocean models are one of the most effective tools to study Internal Waves compared to

38   theoretical methods, in-situ observations, and laboratory investigations. The ocean models with the

39   hydrostatic balance approximation have been used to explore the regional circulation and tide dynamics

40   across the stratified ocean. The hydrostatic balance manages to take the large-to-mesoscale scales into

41   consideration due to the fairly high accuracy (Marshall et al., 1997b; Chen et al., 2003; Shchepetkin and

42   McWilliams, 2005; Ko et al., 2008). However, In the hydrostatic balance scheme, omitting some essential

43   terms in the vertical momentum equation results in the inapplicability of the nonhydrostatic dynamics

44   (Lai et al., 2010). For example, the subsequent steepening of the internal tides and the later high-

45   frequency nonlinear ISWs forming cannot be depicted by a hydrostatic modelling where only internal

46   jumps are formed but no soliton appears (Li, 2010), because the strong vertical current with its order of

47   magnitude equals the horizontal one via the scale analysis method (Marshall et al., 1997a). In other words,

48   the three-dimensional Navier-Stokers equations should be considered thoroughly. It is indispensable for

49   simulating the nonlinear and large amplitude ISWs to develop a nonhydrostatic ocean model in

50   consideration of nonhydrostatic dynamics.

51   A robust ocean model with nonhydrostatic dynamics realizations should satisfy two requirements

52   synchronously at least: 1) The high enough accuracy of meso-to-big scales simulation must be under

53   guarantee, such as large-scale wind-induced circulation and mesoscale eddies reconstructed and mainly

54   influenced by the hydrostatic balance; 2) Meanwhile, it is the concerned small-meso scales with the

55   higher spatial and temporal resolution that are resolved finely under the nonhydrostatic balance, for

56   instance, there is the simulation being able to describe the cradle-to-grave process for the tide-topography

57   interactions, the dispersive effects and nonlinear steepening of baroclinic tides, and the breaking and

58   dissipation of strong nonlinear ISWs. The nonhydrostatic simulation can apply to the small-to-big scales

across the stratified ocean simultaneously, which is identified as one of the main directions for research and development of the nonhydrostatic ocean model. In reality, there have been some nonhydrostatic ocean models or ones considering nonhydrostatic dynamics coming out in the past decades, such as MITgcm (Marshall et al., 1997a;1997b;1998), SUNTANS (Fringer et al., 2006), and ROMS (Kanarska et al., 2007). All above have been used to realize a series of two or three-dimensional nonhydrostatic numerical studies, including the instability of small-scale flows in the laboratory experiment (Lai et al., 2010; Li et al., 2022), Internal Solitary Waves in the continental shelves (Vlasenko et al., 2010, Zeng et al., 2019) and the hydraulic Lee wave around the seamount (Kanarska et al., 2007; Liu et al., 2016). Nevertheless, the primary reason why there is still no widespread use for the nonhydrostatic ocean model is that the nonhydrostatic solution to an extensive sparse linear equation is too demanding to solve directly for the 3-D oceanic environment. That usually demands large amounts of iteration times, fast convergent speed, and PC storage occupation. For this reason, Ai and Ding (2016) employed a novel model grid arrangement to render the sparse linear equation discretized form simpler to solve where the bottom-fitted coordinate ensures the homogeneous boundary condition. Moreover, the numerical errors can be avoided via the immersed boundary method to treat uneven bottoms in the calculation of the baroclinic pressure force (Ai et al., 2021). Generally, whether the boundary conditions are matched with the whole nonhydrostatic algorithm can shape the performance of complex nonhydrostatic dynamics in the regional ocean model. In addition, the different kinds of sub-grid parameterization schemes have a profound impact on the model performance with a necessity for appropriate ones to be assessed, and most of these model codes are seldom shared or of open source. Supposing we develop a nonhydrostatic ocean model based on an original hydrostatic framework model. In that case, the nonhydrostatic dynamics module should involve a complete vertical momentum equation. Some terms associated with the vertical velocity are required to be complemented simultaneously in the other equation. Besides, based on the idea of the fractional step method (Press et al., 1988; Armfield and Street, 2002), the total pressure is to be decomposed into hydrostatics and nonhydrostatic components (Marshall et al., 1997a; Lai et al., 2010). The former corresponds to the result of hydrostatic balance, and the divergence for intermediate velocity limits the latter to correct the local velocity fields called the "pressure correction" method (Stansby and Zhou, 1998; Fringer et al., 2006; Kanarska et al., 2007; Lai et al., 2010). With these methods, the nonhydrostatic dynamics simulation can be fulfilled economically comparatively in harmony with the original physical framework as an extension of the hydrostatic ocean model.

89   In this context, we have implemented the nonhydrostatic dynamic algorithm into an Oceanic

90   Regional Circulation and Tide Model (hereafter ORCTM) and demonstrated its capability and

91   performance of reproducing the life cycle of nonlinear internal solitary waves in distinct hydrodynamic

92   environments. The rest of the paper is organized as follows. In Section 2, the basic framework of ORCTM

93   including control equations, open boundary conditions, and nonhydrostatic algorithms is described. In

94   Section 3, a series of numerical validation experiments results are presented, aiming at the simulation of

95   the overall processes of the internal solitary waves. In the last section, we have some further discussions

96   and come to conclusions.

97   **2. Model Development**

98   The Max Planck Institute Ocean Model (MPI-OM) is a global ocean circulation and tide model based

99   on the ocean primitive equations discretized on the orthogonal curvilinear Arakawa-C grid with

100   hydrostatic balance approximation (Marsland et al., 2003; Chen et al., 2005). Rooted from MPI-OM, in

101   this paper, an oceanic regional circulation and tide model (ORCTM) has been developed to realize the

102   simulation for nonhydrostatic internal solitary waves modelling, which will be referred to hereafter as

103   ORCTM version 1.0. The z-level grid applied has the partial filled cell capability to adjust the distance

104   of the vertical grid on seabed for fitting into the realistic terrain, and the tidal forcing flow can be

105   implemented via a relaxation scheme at the open boundary with an area of sponge layers. It is under the

106   laws of the Boussinesq, rotating and fully nonlinear Navier–Stokes fluid that ORCTM can be used to

107   reproduce and explore the nonhydrostatic dynamics such as large-amplitude ISWs, nonlinear tidal

108   internal waves, and downwelling and upwelling processes of real oceans.

109   **2.1. Control Equations**

110   The three-dimensional ocean primitive control equations involve the momentum, continuity,

111   potential temperature, salinity, and density equations given as follows.

$$\frac{\partial u}{\partial t} + u\frac{\partial u}{\partial x} + v\frac{\partial u}{\partial y} + w\frac{\partial u}{\partial z} - fv + \tilde{f}w = -\frac{1}{\rho_c}\frac{\partial P}{\partial x} - g\frac{\partial \varsigma}{\partial x} + F_{Vx} + F_{Hx} + \mathcal{F}_x \tag{1}$$

$$\frac{\partial v}{\partial t} + u\frac{\partial v}{\partial x} + v\frac{\partial v}{\partial y} + w\frac{\partial v}{\partial z} + fu = -\frac{1}{\rho_c}\frac{\partial P}{\partial y} - g\frac{\partial \varsigma}{\partial y} + F_{Vy} + F_{Hy} + \mathcal{F}_y \tag{2}$$

$$\frac{\partial w}{\partial t} + u\frac{\partial w}{\partial x} + v\frac{\partial w}{\partial y} + w\frac{\partial w}{\partial z} - \tilde{f}u = -\frac{1}{\rho_c}\frac{\partial P}{\partial z} - \frac{\rho}{\rho_c}g + F_{Vz} + F_{Hz} + \mathcal{F}_z \tag{3}$$

$$\frac{\partial u}{\partial x} + \frac{\partial v}{\partial y} + \frac{\partial w}{\partial z} = 0 \tag{4}$$

$$\frac{\partial \theta}{\partial t} + u\frac{\partial \theta}{\partial x} + v\frac{\partial \theta}{\partial y} + w\frac{\partial \theta}{\partial z} = F_{V\theta} + F_{H\theta} + Q_\theta \tag{5}$$

$$\frac{\partial S}{\partial t} + u\frac{\partial S}{\partial x} + v\frac{\partial S}{\partial y} + w\frac{\partial S}{\partial z} = F_{VS} + F_{HS} + Q_s \tag{6}$$

$$\rho = \rho(\theta, S, P) \tag{7}$$

112   In the local cartesian framework of reference on the rotating earth for a geophysical flow, t is the

113   time; $\partial/\partial t$ is the time partial derivative; x, y and z axes direct eastward, northward, and upward

114   respectively; The horizontal velocity vector is $\boldsymbol{u_h} = (u, v)$; w is the vertical velocity. With the

115   linearized kinematic boundary condition and the fresh water forcing term Q_ς from the evaporation and

116   precipitation (Marsland et al., 2003), the free surface elevation equation can be proposed as follows.

$$\frac{\partial \varsigma}{\partial t} = -\nabla_h \cdot \int_{-H}^{\varsigma} \boldsymbol{u}_H dz + Q_\varsigma \tag{8}$$

117   ς is the change of the free surface elevation; P, θ, and S are pressure, potential temperature and

118   salinity; ρ_c is the reference density of sea water. The first and second Coriolis parameters are $f =$

119    $2\Omega\sin\varphi$ and $\tilde{f} = 2\Omega\cos\varphi$, where Ω is the rotational angular speed and φ is the geographic latitude.

120   ∇_H is the horizontal divergence operator; Q_θ and Q_s are source or sink terms about potential

121   temperature and salinity. The equation of seawater state is the polynomial form for the density ρ

122   advocated by the Joint Panel on Oceanographic Tables and Standards (Fofanoff and Millard, 1983). The

123   additional forcing term vector $\boldsymbol{\mathcal{F}} = (\mathcal{F}_x, \mathcal{F}_y, \mathcal{F}_z)$ can consider tidal potential forcing. The horizontal eddy

124   viscosity vector is $\boldsymbol{F}_H = (F_{Hx}, F_{Hy}, F_{Hz})$ described with the scale-dependent biharmonic formulation

125   (Wolff et al., 1997; Marsland et al., 2003), and the horizontal diffusivity terms of temperature and salinity

126   are $F_{H\theta}$ and F_{HS} supporting the harmonic forms. Besides, the vertical eddy viscosity vector is $\boldsymbol{F}_V =$

127   (F_{Vx}, F_{Vy}, F_{Vz}) and eddy diffusivity terms are $F_{V\theta}$ and F_{VS}. Here, the vertical eddy turbulent frictions

128   are specified to depend on the Richardson number Ri via the modified PP81 parameterization scheme

129   (Pacanowski and Philander, 1981). The viscous terms all above are expressed as

$$\boldsymbol{F}_H = -\nabla_h \cdot (B_H \nabla_h \Delta \boldsymbol{u}), \quad \boldsymbol{F}_V = \frac{\partial}{\partial z}\left(A_V \frac{\partial \boldsymbol{u}}{\partial z}\right) \tag{9}$$

$$F_{\chi H} = D_H \Delta \gamma, \quad F_{\chi V} = \frac{\partial}{\partial z}\left(D_V \frac{\partial \chi}{\partial z}\right), \quad \chi = \theta, S \tag{10}$$

$$A_V^{n+1} = (1 - \lambda)A_V^n + \lambda(A_{V0}(1 + \alpha \cdot Ri)^{-2} + A_w + A_b) \tag{11}$$

$$D_V^{n+1} = (1 - \lambda)D_V^n + \lambda(D_{V0}(1 + \alpha \cdot Ri)^{-3} + D_w + D_b) \tag{12}$$

$$Ri = \frac{N(z)^2}{(\partial u/\partial z)^2 + (\partial v/\partial z)^2} \tag{13}$$

130 where $\Delta = \nabla_h \cdot \nabla_h$ is the horizontal Laplace operator; B_H and D_H are parameterized with the horizontal

131 grid resolution; $N(z)$ is the buoyancy frequency. A_V^{n+1} and D_V^{n+1} are updated on formulas (11) and (12)

132 with the time relaxation coefficient λ at every time step. Apart from the background viscous coefficients

133 A_b and D_b due to internal waves breaking, the modified PP81 scheme also considers the wind-induced

134 turbulent coefficients A_w and D_w associated with the local mixed layer depth and 10m wind speed

135 (Marsland et al., 2003). Here, the constant number α is set to be 5. And the adjustable parameters A_{V0}

136 and D_{V0} can be determined by estimating energy flux at every grid point. As for the boundary condition,

137 the slip conditions are specified at surface and bottom boundaries where the wind stress τ_w is based on

138 the model input, and the bottom drags τ_b are described by linear and quadratic functions (Arbic and Scott,

139 2008). The top and bottom boundary conditions can be written as

$$\tau_w/\rho_c = A_V \frac{\partial \boldsymbol{u_h}}{\partial z}\Big|_{z=\varsigma}, \qquad \tau_b/\rho_c = A_V \frac{\partial \boldsymbol{u_h}}{\partial z}\Big|_{z=-H} = \left(\gamma + C_d\sqrt{u^2 + v^2}\right)\boldsymbol{u_h} \tag{14}$$

140 Where γ and C_d are the bottom friction and drag coefficients representing the linear and quadratic

141 relation expressions, respectively.

2.2. Settings of Open Boundary Condition

143 It is fundamental for the regional model to be configured by an open boundary condition that avoids

144 reflection waves effectively so that the outward waves can freely flow through the boundaries.

145 Meanwhile, external inputs such as tidal waves can stably force the model domain through the boundaries,

146 satisfying the need for consistency in hydrodynamics and computational mathematics. Here, we use the

147 relaxation boundary conditions with sponge layers consulting Zhang et al. (2011) that can dampen the

148 reflection waves back into the interior domain and refrain from the sharp gradients of water properties

149 caused by the prescribed values on the boundaries. Specifically, we add a relaxation term $M(x, y, z, t)$

150 formularized with the exponential function in the specified sponge zones. At each time step, the model

151 variables are updated with an explicit scheme expressed as

$$M(x, y, z, t) = -\left(\frac{m(x, y, z, t) - m_b(x, y, z, t)}{\tau}\right) \cdot e^{-\delta}, \quad m = u, v, w, \theta, S \tag{15}$$

$$m = (1 - \beta)m^* + \beta m_b, \qquad \beta = \frac{\Delta t e^{-\delta}}{\tau}, \qquad \delta = \frac{4r(x, y)}{L_{sp}} \tag{16}$$

152 In the formulas (15) and (16), m_b is the boundary value of requisite model variable including

153   velocity, potential temperature, and salinity; m is the corresponding relaxation result in the interiors;

154   m^* is the intermediate variable; r is the distance from the boundary; Δt is the model time step. Here, it

155   should be noted that τ and L_{sp} are artificially prescribed adjustment parameters referring to the time-

156   scale coefficient and the thickness of the sponge relaxation layers. The model target variables over the

157   sponge layer will relax exponentially to the boundary values through the relaxation term, where

158   relaxation is modulated by τ and L_{sp} in the exponential shape. To restrain the reflection of outflow

159   current, τ and L_{sp} need to be determined in advance via estimating the energy flux of internal signals

160   through the boundaries. This open boundary relaxation condition is suitable for the numerical study of

161   the large-amplitude ISWs so that the outward strong, nonlinear, and nonhydrostatic wave and current

162   signals will dampen gradually.

163   **2.3. Implement of Nonhydrostatic Algorithms**

164   According to the momentum equations (1) to (3), the total pressure P consists of sea surface

165   pressure p_s, hydrostatic pressure p_h, and nonhydrostatic pressure p_{nh} given as follows.

$$P = p_s(x, y) + p_h(x, y, z) + p_{nh}(x, y, z) \tag{17}$$

$$\frac{\partial p_h}{\partial z} = -\rho g \tag{18}$$

166   It is negligible for the change of sea surface pressure term p_s to impact on the water column if the

167   external atmospheric forcing is excluded. Hydrostatic pressure p_h can be calculated from the hydrostatic

168   balance equation (18), and the vertical momentum equation (3) at this stage becomes

$$\frac{\partial w}{\partial t} = -\frac{1}{\rho_c}\frac{\partial p_{nh}}{\partial z} + \frac{\partial}{\partial z}\left(A_V \frac{\partial w}{\partial z}\right) - \nabla_h \cdot (B_H \nabla_h \Delta w) + \tilde{f}u - \boldsymbol{u} \cdot (\nabla \cdot w) \tag{19}$$

169   Where the left term refers to the local time rate of change, and the right term is the sum of the other forces

170   without the additional forcing term vector. Compared with Eq. (18), the vertical momentum equation (19)

171   can be also called nonhydrostatic balance equation. Furthermore, with the idea of the fractional step

172   method (Press et al., 1988; Kanarska et al., 2007), the intermediate velocity field $\tilde{\boldsymbol{u}} = (\tilde{u}, \tilde{v}, \tilde{w})$ will be

173   updated via the nonhydrostatic pressure p_{nh}^n gradients, which can be obtained via the Eqs. (20) to (22)

174   discretized as follows.

$$\frac{\tilde{u} - u^n}{\Delta t} = -G_x - \frac{1}{\rho_c}\frac{\partial p_{nh}^n}{\partial x} \tag{20}$$

$$\frac{\tilde{v} - v^n}{\Delta t} = -G_y - \frac{1}{\rho_c}\frac{\partial p_{nh}^n}{\partial y} \tag{21}$$

$$\frac{\widetilde{w} - w^n}{\Delta t} = -G_z - \frac{1}{\rho_c}\frac{\partial p_{nh}^n}{\partial z} \tag{22}$$

175 Where the superscript n means the current time step and the vector $\boldsymbol{G} = (G_x, G_y, G_z)$ represents the sum

176 of advection term, Coriolis term, eddy viscosity term, and hydrostatic pressure gradients term. The

177 discretized partial equations (23) to (25) are established subsequently under the relationship between the

178 nonhydrostatic pressure perturbation p_{nh}' gradients and the next time step $n+1$ velocity field. Then

179 nonhydrostatic pressure at next time step is defined as equation (26) in the light of the pressure correction

180 method. To acquire nonhydrostatic pressure perturbation the continuity equation (4) needs to be

181 substituted into Eqs. (23) to (25) to eliminate the following time step $n+1$ velocity field with the three-

182 dimensional Poisson equation (27) left, which demonstrates that the nonhydrostatic pressure depends on

183 the vanishes of the divergence-free velocity fields.

$$\frac{u^{n+1} - \tilde{u}}{\Delta t} = -\frac{1}{\rho_c}\frac{\partial p_{nh}'}{\partial x} \tag{23}$$

$$\frac{v^{n+1} - \tilde{v}}{\Delta t} = -\frac{1}{\rho_c}\frac{\partial p_{nh}'}{\partial y} \tag{24}$$

$$\frac{w^{n+1} - \widetilde{w}}{\Delta t} = -\frac{1}{\rho_c}\frac{\partial p_{nh}'}{\partial z} \tag{25}$$

$$p_{nh}^{n+1} = p_{nh}^n + p_{nh}' \tag{26}$$

184 The Poisson equation (27) can be discretized into a linear matrix Eq. (28) where the right-hand side

185 $\boldsymbol{B}$ is determined by the divergence of the intermediate velocity field. The adjoint matrix $\boldsymbol{A}$ represents the

186 discrete three-dimensional Laplacian operator with a size of the number of model cells. Their specific

187 discrete processes are introduced in Appendix A.

$$\frac{\partial^2 p_{nh}'}{\partial x^2} + \frac{\partial^2 p_{nh}'}{\partial y^2} + \frac{\partial^2 p_{nh}'}{\partial z^2} = \frac{\rho_c}{\Delta t}\left(\frac{\partial \tilde{u}}{\partial x} + \frac{\partial \tilde{v}}{\partial y} + \frac{\partial \widetilde{w}}{\partial z}\right) \tag{27}$$

$$\boldsymbol{A}p_{nh}' = \boldsymbol{B} \tag{28}$$

$$\nabla p_{nh}' \cdot \boldsymbol{n} = 0 \tag{29}$$

188 The proper boundary conditions need to be given to solve this Poisson equation (27). Here, the

189 homogeneous Neumann boundary condition at the solid boundaries, also called the Zero-gradient

190 condition (29), is used with good compatibility with the no flux normal to slope, where $\boldsymbol{n}$ is the normal

191 unit vector (Marshall et al., 1997a). We assume that nonhydrostatic dynamic processes are weak enough

192 at the sea surface and open boundaries. In other words, the input signals through the boundaries are

193 dominantly hydrostatic with nonhydrostatic pressure perturbation close to zero. The nonhydrostatic

194 dynamic framework is restricted to the interiors. Hence, the Zero-gradient condition is utilized to hold

195 back sharp nonhydrostatic pressure gradients at the open boundaries. With the above boundary conditions,

196 this linear system (28) can be solved via the Krylov subspace method with PETSc's assistance on parallel

197 computers under the standard MPI-based framework (Balay et al., 2020). Besides, a highly efficient

198 method need to be devised to precondition the huge and sparse matrix A. Here, the multigrid

199 preconditioner (Smith et al., 1996) and flexible generalized minimal residual algorithm (Saad, 1993) are

200 employed in numerical validation experiments in this paper to minimize computational costs.

201 **3. Model applications and assessments**

202   In this section, we present a series of ideal numerical validation experiments to explore the

203 correctness and compatibility of nonhydrostatic algorithms together with ORCTM. In allusion to the

204 internal solitary wave dynamics, these test cases range from laboratory-scale cases in an enclosed tank

205 to field-scale ones like the northern South China Sea with open boundaries. The first case is the lock-

206 exchange problem as the preliminary validation. The second to fourth cases are designed to explore the

207 nonlinear evolution of internal solitary waves induced by their interactions with the changing terrain.

208 The last one is the generated nonlinear internal waves case in a double-ridge environment analogous to

209 the Luzon Strait, which aims at the generation and disintegration of nonlinear internal waves to examine

210 the effectivity of open tidal forcing condition module under the nonhydrostatic algorithms. Analyses of

211 all test experiments above indicate that ORCTM can reproduce nonlinear and nonhydrostatic internal

212 solitary waves in different oceanic environments, which exhibits the robustness and reliability of this

213 nonhydrostatic ocean model.

214 **3.1. The lock-exchange problem**

215   When the shear currents flow between the two different density fluids, the Kelvin-Helmholtz

216 instability (hereafter K-H instability) will appear to cause turbulent diapycnal mixing (Lawrence et al.,

217 1991; Cushman-Roisin, 2005). The perturbation on the interface gradually develops and stimulates

218 numerous small eddies due to energy dissipation. The magnitude order of vertical flow is comparable to

219 the horizontal one so the nonhydrostatic effect matters throughout the whole process. We set a rectangle

220 enclosed tank separated by a vertical board in the middle at the x-axis origin. Both sides of the tank are

221 separately filled with two different density fluids in Fig. 1a. The gravitational adjustment will proceed

222 when the central board is disengaged just like a lock gate. Here, we refer to the previous configurations

223 (Härtel et al., 2000; Fringer et al., 2006; Lai et al., 2010) as a 2-D problem. The horizontal length L is set

224 to 50 cm, and the static water height is 10 cm without topographic change in the tank. The grid resolution

225 is 0.001 m in horizontal and vertical directions. Several sensitivity experiments were explored to reduce

226 the dissipations out of solid boundary friction, so the bottom friction coefficients are finally set to zero;

227 both A_{V0} and D_{V0} in formulas (11) and (12) are 2×10^{-6} m^2 s^{-1}. Besides, water density averages are

228 calculated based on the prescribed salinity difference on the left and right sides of the tank $\rho_l = 1023.05$

229 kg m^{-3} and $\rho_r = 1026.95$ kg m^{-3}.
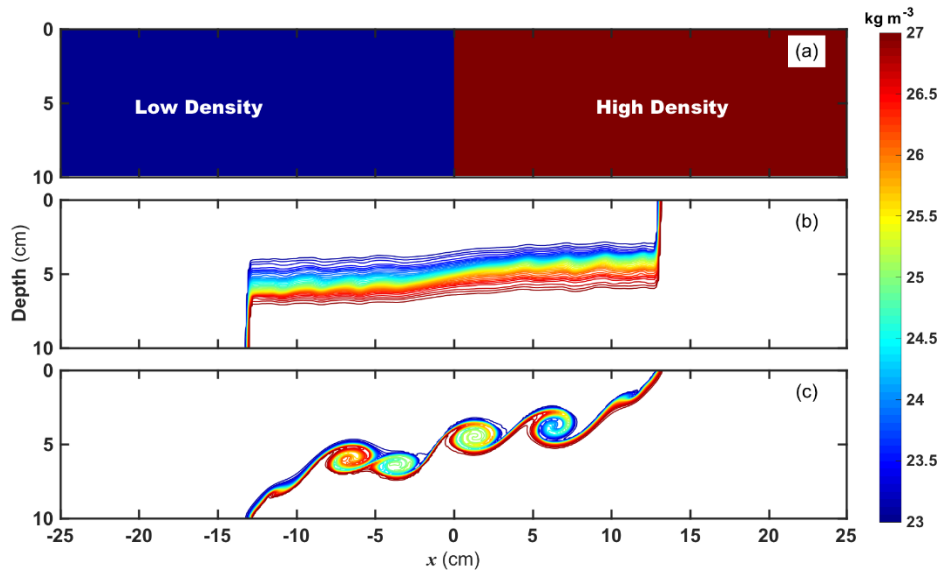
230

231 Figure 1. (a) The initial density σ (hereafter the same expression) field of the lock-exchange case, and

232 their contour plots of density at $t = 4.5$ s where the contour interval is 0.1 kg m^{-3} under the hydrostatic

233 (a) and nonhydrostatic (b) model framework.

234   The K-H instability process grows rapidly with good eddies reconstruction and outstanding waves

235 breaking. In contrast in that model configuration, we also run the same configuration experiment above

236 but under the hydrostatic balance scheme. Figures 1b and 1c show the results of density σ (define $\sigma =$

237 $\rho - 1000$ kg m^{-3}) at the same time under the hydrostatics and nonhydrostatic balance framework. The

238 comparison proves that the K-H instability cannot proceed resulting from the inapplicability of the

239 hydrostatics balance. The perturbation on the density interface is so tiny that the density fronts cannot

240 evolve in the upper and lower layer, so the mixing caused by the overturning and shear is too weak to be

241 seen. On the contrary, via the nonhydrostatic scheme, the eddies can proliferate with energy dissipation

242 due to the associated shear on the perturbation, vigorously mixing the high and low-density water on the

243 interface. More specifically, the energy is transmitted to the small-scale eddies across the density fronts

244 due to dispersion and nonlinearity.

245   The evolution process of K-H instability is shown in Fig. 2. It is out of gravitational adjustment that

246 the density fronts movement accompanies with the heavy water in the bottom and light one in the upper

247 moving to the left and right, respectively, causing a velocity shear field and clockwise rotating interface

248 in Fig. 2a. The shear strength gradually increases until breaking the critical point of restoring force that

249 depends on the density gradient, and later a series of eddies grow from the middle to both sides of the

250 tank with the turbulent rolling and overturning. These eddies mix the water body with high density at the

251 bottom and the upper one with low density, forming multiple considerable density mixing areas in Figs.

252 2b and 2c. When the bottom density flow is reflected on the left wall, the similar adjustment process

253 begins to develop in reverse of Figs. 2d and 2e, but the strength of subsequent eddies is significantly

254 weakened due to energy dissipation.
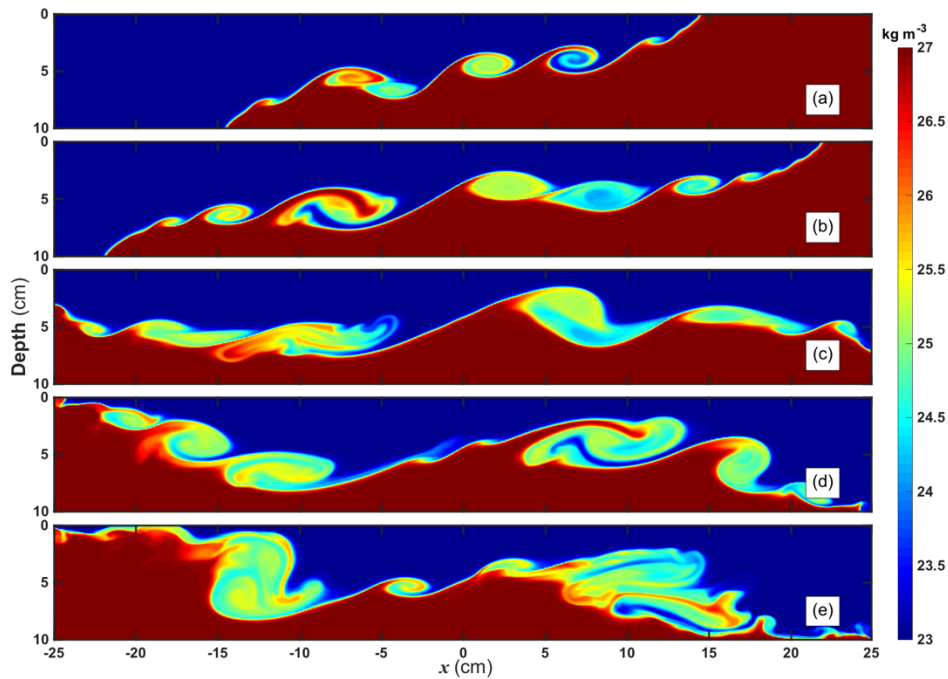
255

256   Figure 2. Density field evolution at t = (a) 5.0, (b) 7.5, (c) 10.0, (d) 12.5, and (e) 15.0 s

257   These density distributions display the generation of density fronts and numerous eddies throughout

258 the gravitational adjustment process. Based on the point of energy dynamics, the gravitational potential

259 energy (PE) is converted to the kinematical energy (KE) for the water parcel, while the total energy

260 dissipates continuously in the tank. Here, KE and PE of the entire 2-D tank are calculated from the

261   following formulas.

$$KE = \int_0^L \int_{-H}^{\varsigma} \frac{1}{2}\rho(u^2 + w^2)dxdz \qquad (30)$$

$$PE = \int_0^L \int_{-H}^{\varsigma} \rho gzdxdz \qquad (31)$$

262   The three curves show the fluctuation of PE, KE, and total energy during the K-H instability

263   simulation in Fig. 3. The PE and KE correspond to the maximum and zero due to the initial density

264   distribution and static field in Fig. 3a. Afterward, the PE declines sharply with an opposite change of KE.

265   Both rates of change are almost the same based on the curve slopes, which demonstrate that PE is

266   converted to KE, reaching mutual peaks of about 9.5 s at the end of the first gravitational adjustment.

267   From then on, both of them still maintain the opposite trends with an oscillation of roughly 25 s. It is

268   worth noting that all kinds of energy exhibit a downward trend with their oscillation period increasing

269   steadily due to energy dissipation so that KE will drop to zero and PE and total energy (PE+KE) will

270   reach the constant in the end. The results above are equivalent to the previous works (Harel et al., 2000;

271   Fringer et al., 2006; Lai et al., 2010), implying the correctness of the nonhydrostatic dynamic module.
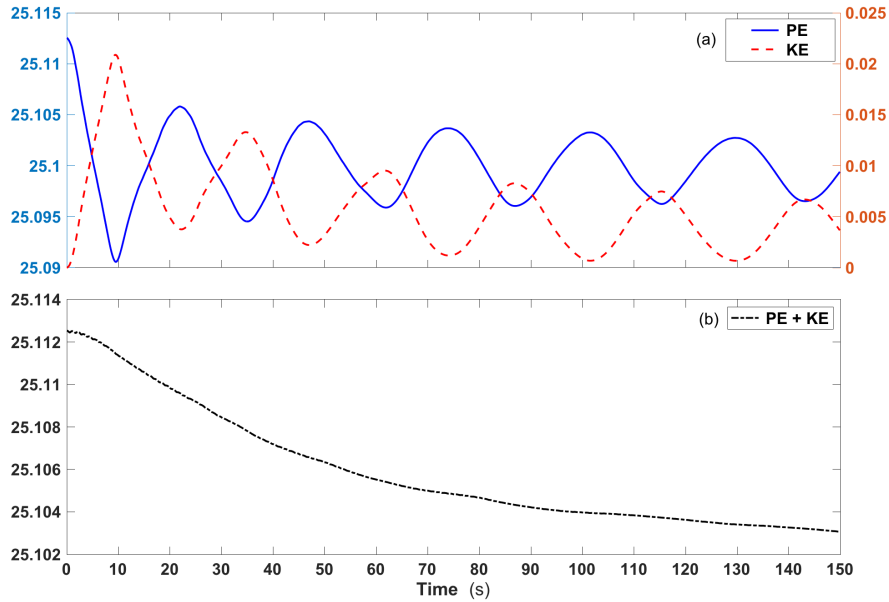
272

273   Figure 3. (a) The timeseries of the kinematical (red dashed line), potential (blue solid line) energy, and

274   (b) the same as total (black dotted line) energy (units: kg m^2 s^{-2}).

3.2. Internal Solitary Wave in a tank

Internal solitary wave activities are ubiquitous in the ocean with strong nonlinearity and nonhydrostatic effect. Laboratory experiments are usually carried out to study the ISWs to make up for the defects of field observations. The numerical ISWs experiment in a laboratory-scale background needs to be combined simultaneously (Grue et al., 2000). We follow the previous experimental configuration (Ma et al., 2019). A schematic diagram of the ISW experiment is given in Fig. 4. The tank length is 2.0 m with the x-axis origin located on the left; the static height is 10 cm without topographic change; the horizontal and vertical resolutions are 2×10^{-3} and 1×10^{-3} m; both bottom friction and drag coefficients are set to 3×10^{-3} with the effect of a fairly robust friction to the ISW; A_{V0} and D_{V0} are same as the experiment configuration in section 3.1. Here, a gravity collapse method is used to generate the depression ISW. Specifically, the low- and high-density fluids initially fill the upper and lower layers of the tank with the collapse area on the left side. The collapse height and width are 5.0 cm and 4.0 cm. Water density averages are calculated in the upper and lower layer with $\rho_1 = 1003.62$ kg m^{-3} and $\rho_2 = 1026.95$ kg m^{-3}. Additionally, the diagnostic module is employed to characterize the high-frequency variation. The high-frequency outputs are positioned at points $x = 0.4, 0.8, 1.2$, and 1.6 m with a time interval of 0.05 s.
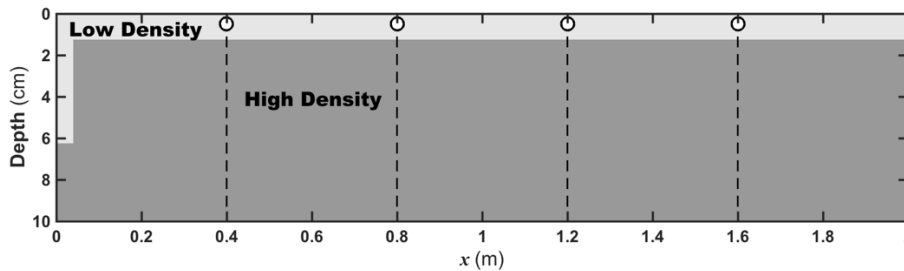
Figure 4. Schematic diagram of ISW case. The light and dark gray indicate the low- and high-density water with 1003.62 kg m^{-3} and 1026.95 kg m^{-3}, where four white dots refer to the high-frequency output points.

Figure 5 distinctly illustrates the evolution of the ISW packet in the tank based on the pycnocline fluctuation. The isopycnic of 1026 kg m^{-3} can characterize the maximum strength of depression ISW in Fig. 5a. The eastward starting wave packet originated from the west gravity collapse area comprises the depression heading wave and several tail waves whose amplitudes decreases successively. The heading wave with the maximum amplitude propagates much faster than the tails behind so that the distance

300 expands promptly between them. As is exhibited in Table 1 about the heading wave characteristics at the

301 four locations, we find the wave amplitude with almost little change and then a slight fluctuation but no

302 more than 0.1 cm after $x = 0.8$ m. The quantitative evaluation of the wave speed based on the slope of

303 the blue dashed area in Fig. 5b reveals that the wave speed increases slowly after $x = 0.2$ m but with its

304 increment less than 0.01 m s^{-1}. Those above indicate that the starting ISW packet are still at the stage of

305 gravity adjustment before arriving at $x = 0.2$ m and then propagating to the east steadily in our simulation.

306 Besides, the characteristic westward reflected waves (the blue line in Fig. 5a) with the larger amplitude

307 prove that the wave-wave interactions happen between the reflected and starting tail waves.
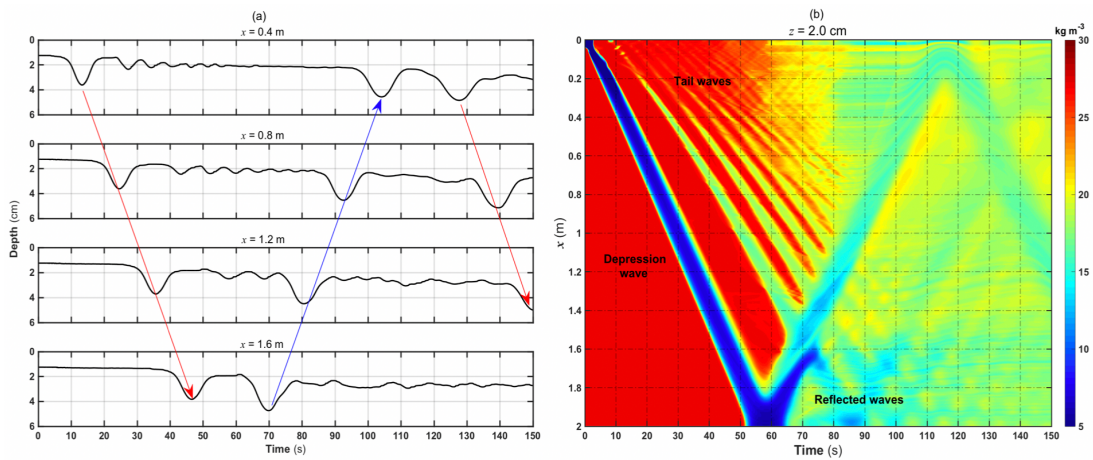
308

309 Figure 5. (a) The density timeseries of 1026 kg m^{-3} at the four high-frequency output locations from the

310   west to east. The left red and blue arrow lines indicate the eastward and westward waves, and the right

311   red means the eastward reflected waves from the channel start. (b) Hovmöller diagram showing the

312   density σ at $z = 2.0$ cm where the time interval is 0.1 s.

313

314   Table 1 The characteristics of the depression heading wave at the four points

location (x/cm) parameters	0.4	0.8	1.2	1.6
amplitude (a/cm)	2.369	2.362	2.392	2.469
characteristic wavelength (L/cm)	19.632	21.643	23.206	25.822
nonlinearity (ε)	0.237	0.236	0.239	0.250
dispersion (μ)	0.259	0.213	0.186	0.150

315
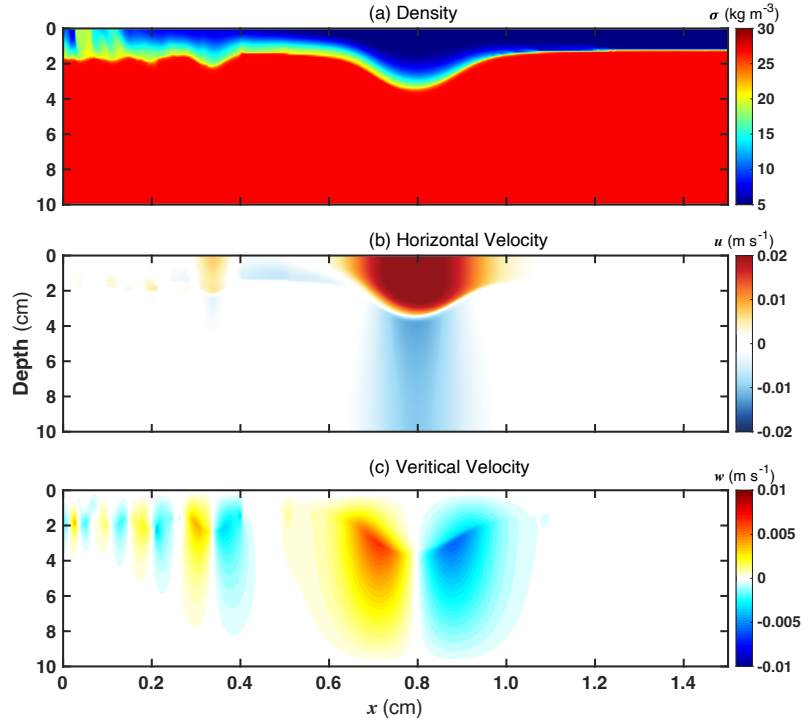
316

317   Figure 6. From top to bottom, density, horizontal and vertical velocity fields of the ISWs at t = 24.5 s.

318   We select a snapshot result for characteristic verification shown in Fig. 6 when the heading wave

319   arrives at around x = 0.8 m. The strongest horizontal velocity of the depression wave is 0.023 m s^{-1}, and

320   the vertical flow can reach up to 0.0065 m s^{-1}. The characteristic velocity fields are in line with the

321   clockwise structure of a theoretical depression internal solitary wave. Furthermore, the nonlinearity $\varepsilon =$

322   a/h and dispersion $\mu = (h/\lambda)^2$ are calculated at the different locations in Table 1 where a, h, and λ

323   are the amplitude, water height, and characteristic wavelength. The KdV model (Benjamin, 1966)

324   described in Appendix B is utilized to predict theoretical waveforms at the four locations. The

325   comparison depicted in Fig. 7 demonstrates that the results are more consistent with the KdV model

326   rather than m-KdV model. According to the nonlinearity ε from Michallet and Barthélemy (1998), the

327   small and large-amplitude ISW can be classified when $\varepsilon <$ 0.05 and $\varepsilon >$ 0.05, respectively. Whereas

328   the application of the KdV model requires a balance between the weak nonlinearities and dispersion

329   (Ono, 1975), which namely needs satisfy this condition $\mu = O(\varepsilon) \ll 1$. Despite the large-amplitude

330   waves simulated from our model with $\varepsilon >$ 0.05, the nonlinearity and dispersion are of the same order

331   and small enough that the heading wave can be deemed under weak nonlinearity. Those can explain this

332   reason why the waveforms are better described by the KdV model. Therefore, analyses of the theoretical

333   model indicate that the simulation of internal solitary wave can be fulfilled authentically using our

334   nonhydrostatic model.
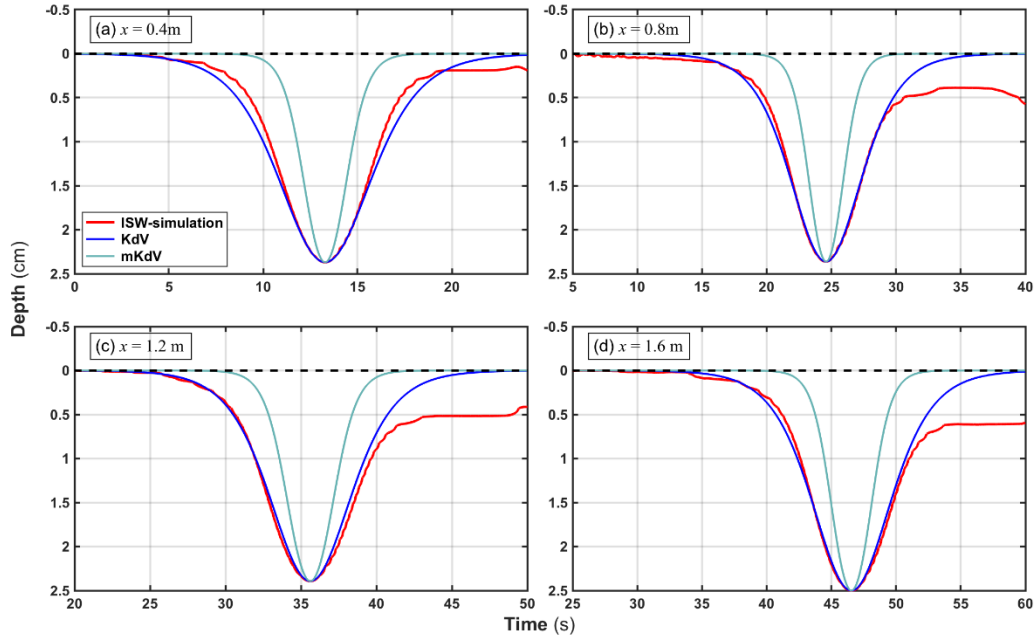
Figure 7. The interface displacement induced by ISW at four high-frequency output locations. The red lines indicate the 1026 kg m^{-3} isopycnic, and the blue and cyan lines represent the KdV and m-KdV model results.

3.3. Internal Solitary Wave shoaling on a Gaussian terrain

Based on the experiment configuration in section 3.2 (also called Exp. 3.2). Here, a slowly varying terrain is implemented to explore the nonlinear evolution of internal solitary wave in this section 3.3 (also called Exp. 3.3), especially the wave shoaling. As shown in Fig. 8, the left half of the Gaussian curve is reserved as the slope-shelf terrain starting between $x = 1.0$ and 1.3 m with a height of 5.0 cm, and then the water depth remains unchanged from $x = 1.3$ to 2.0 m corresponding to the shallow water zone. The high-frequency outputs are acquired during the climbing process of ISWs at points $x = 0.4$, 0.8, 1.0, 1.2, 1.3, 1.4, 1.6, and 1.8 m with the same output interval as Exp. 3.2.
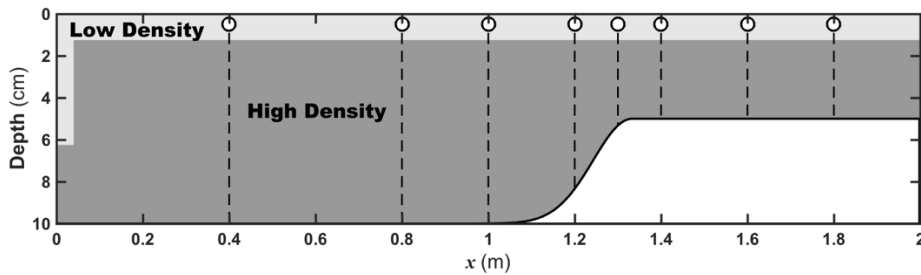
Figure 8. As in Figure 4, but with half-Gaussian topography in the east of the tank, where eight white dots refer to the high-frequency output points.

350   The evolution of the internal solitary waves with varying topography is displayed in Fig.9. The

351   heading ISW holds a stable packet at $x = 0.4$ m and initiates to shoal after reaching $x = 1.0$ m. Afterward,

352   the heading ISW undergoes the topographic change so that the speed of the wave trough is less than the

353   wave rear. Consequently, the contrasting effects on the wave front and wave rear contribute to the former

354   gentle sloping but the latter gradual steepening, which shows a similarity with Vlasenko et al. (2002).

355   Then the closed isopycnic contour mirrors the backward overturning and rolling due to the wave breaking

356   at $x = 1.2$ m in Fig. 9a. Apart from the wave breaking process above, it is also found in Fig. 9b that the

357   reflected waves propagate back to the deep water zone from $x = 1.2$ m. In other words, both the wave

358   breaking and refection attenuate substantially the original depression ISW energy. When arriving at the

359   east of $x = 1.2$ m, the original depression wave past the critical point where the upper layer is thicker than

360   the lower one in Fig. 10a, so an elevation wave springs up in the wave rear. The elevation wave then

361   continues to propagate eastward, which leads to accumulating the high-density water in the upper water

362   increasingly in the right region close to the wall of the tank. Hence, A new collapse area between $x = 1.8$

363   m and the east wall comes into being where the thickness of the upper layer is larger than lower layer.

364   Ultimately, the westward reflected waves including a series of elevation tail waves, are released at $x =$

365   1.6 m. In detail, the first elevation is the leading one with a rank-ordered structure in the rear. After

366   reaching the deep water zone left to 1.3 m, the wave rear begins to steepen and sink, and a depression

367   wave forges behind the wave rear. Namely, the soliton wave passes the critical point inversely due to the

368   wave deepening.
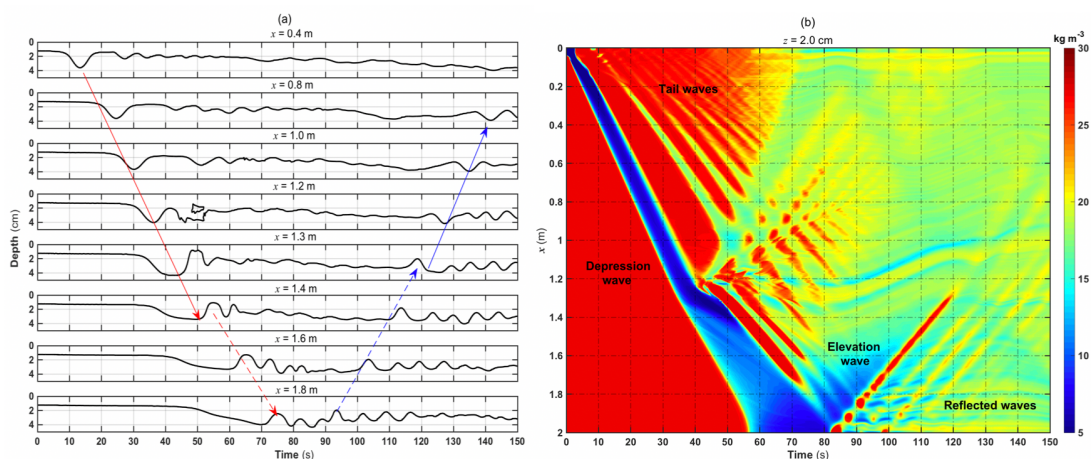
370   Figure 9. As in Figure 5, (a) the solid and dashed arrow lines indicate the depression and elevation

371   waves, and the red and blue mean the eastward and reflected westward waves. (b) Hovmöller diagram

372   showing the density σ at $z = 2.0$ cm.

373   For further exploration of the evolution of the depression wave, the distributions of the vorticity

374   ($\zeta = \partial w/\partial x - \partial u/\partial z$) with velocity vector are depicted in Fig.10. The depression wave core features

375   negative vorticity with an anticyclonic velocity structure before reaching the shelf topography. When the

376   ISW approaches the top of the slope in Figs. 10a and 10b, the vertical shear increases promptly and

377   strengthens the positive vorticity at the bottom. Then the backward overturning springs up between x =

378   1.2 and 1.3 m, marking the ISW entering the breaking instability stage (Helfrich and Melville, 1986) due

379   to the shoaling. At this time, even though wave breaking and reflection render the wave energy

380   dissipation partially, the fraction of the depression wave can reach the shallow water zone, leaving a

381   cyclonic vortex behind above the slope-shelf in Fig. 10c. This partial soliton wave is adjusted

382   instantaneously when the upper layer thickness is more significant than the lower in the light of the

383   boundary of the negative vorticity area in Fig. 10d. As a result, after the reverse situation occurs, the

384   elevation wave begins to emerge at the back of the original wave. Its core corresponds to the positive

385   vorticity with a cyclonic velocity structure. In addition, the vortex from the wave breaking weakens

386   slowly and motivates numerous small-scale waves with high wavenumber propagating to both sides in

387   Figs. 10e and 10f, which is consistent with the propagation characteristics of the reflected waves near x

388   = 1.2 m in Fig. 9b.
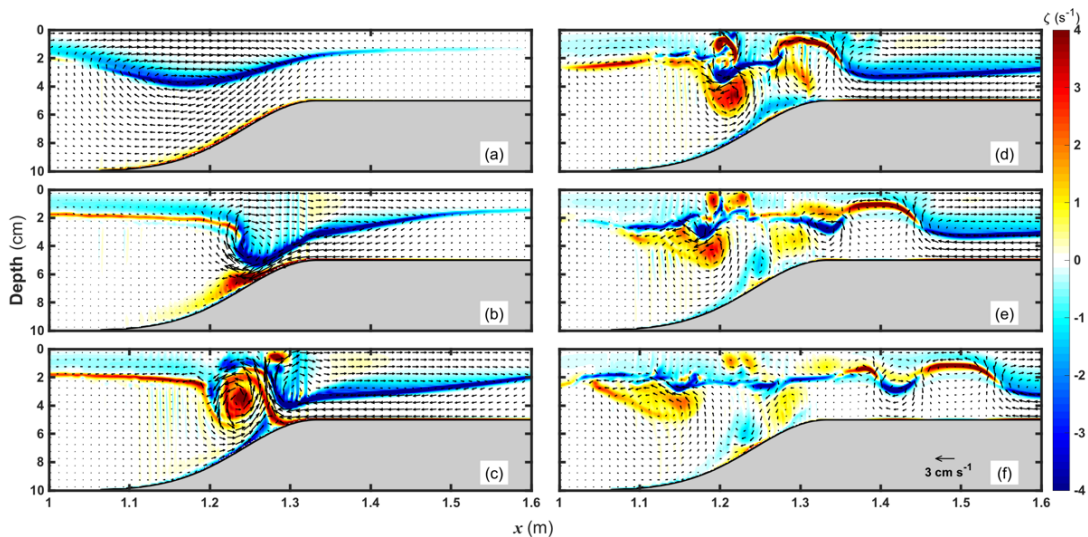
389

390   Figure 10. The shoaling of a depression soliton where the velocity fields (black arrow) and the vorticity results

391   (color) are shown at t = (a) 35, (b) 40, (c) 45, (d) 50, (e) 55, and (f) 60 s.

392   It is also worthy of highlighting the evolution of the reflected westward waves. We also visualize

393   the process of the second reverse situation due to the wave deepening in Fig. 11. It can be noticed that

394   there is a leading elevation wave at $x = 1.4$ m followed by a series of rank-order waves exhibiting a

395   likewise sinusoidal variation. They propagate together to the deep water zone with the wave crest

396   corresponding to positive vorticity. Particularly, the wave train is considered linear approximatively

397   based on the alternated positive and negative vorticity regions, since the cores of these waves almost are

398   located in the middle layer where the nonlinear parameter α is close to zero in terms of the KdV model.

399   As the water depth becomes deeper, the crest of the elevation wave gradually grows down and flattens

400   with the wave rear sinking. The original elevation cannot be maintained in the deep water, transforming

401   into a depression wave with the velocity fields adjusted accordingly.
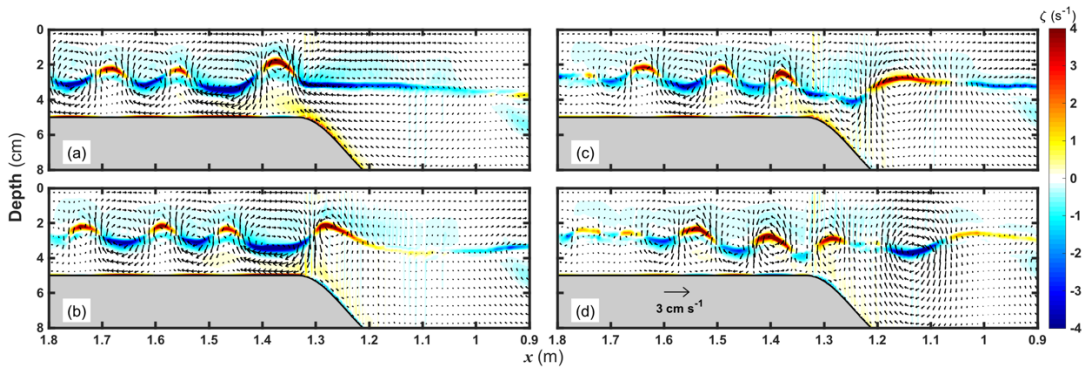
402

403   Figure 11. As in Figure 10, the elevation wave propagates westward to the deep water where the x-axis is inverse

404   for convenience at $t =$ (a) 115, (b) 120, (c) 125, and (d) 130 s.

405   The ISW is not stable enough to coincide with the KdV model after pasting the critical point into

406   the adjustment stage. Hence, we select the two types of soliton results for verification before the reverse

407   situation occurs. The comparison results between theoretical and numerical model are illustrated in Fig.

408   12 at $x = 0.8$ and 1.4 m before the wave shoaling and deepening, respectively. We can find that the

409   depression waveform conforms to the KdV model results before climbing the slope, whereas the

410   elevation is closer to the m-KdV model. Compared with $\varepsilon = 0.233$ at $x = 0.8$ m, the interaction between

411   the ISW and the shoaling topography renders a stronger nonlinearity $\varepsilon = 0.331$ of the elevation heading

412   wave in the shallow water. Namely, the larger wave amplitude ratio in the shallow water results can be

413   characterized with m-KdV theory, which compares well with the conclusions of Michallet and

414   Barthélemy (1998) in a satisfactory way.
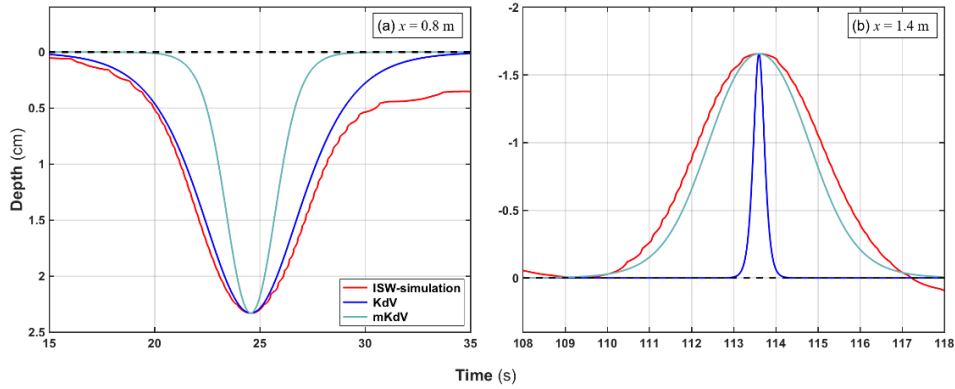
415

416   Figure 12. Wave profiles at x = 0.8 (a) and 1.4 m (b). The left (right) refers to the depression (elevation)

417   heading wave before shoaling (deepening), where the results are plotted with the red line. The blue and

418   cyan lines represent the KdV and m-KdV model results.

3.4. Internal Solitary Wave breaking on a slope.

420   To further characterize a complete breaking and dissipative process of ISWs, we set a linear slope

421   identical to Michallet and Ivey (1999). As is shown in Fig. 13, the tank length is 2.0 m; The height is 15

422   cm with the linear terrain placed on the east side. The model configuration (i.e., spatial resolution and

423   viscous coefficients) is identical to Exp. 3.2, which can ensure the same time step according to Courant-

424   Friedrichs-Lewy (CFL) condition, and the depression ISW is about to be dissipated due to increasing

425   bottom friction at the shelf break. In contrast with Bourgault and Kelley (2004), water density averages

426   are calculated to be ρ_1 =1000.01 kg m^{-3} and ρ_2 =1047.00 kg m^{-3} in the upper and lower layers. Via

427   several sensitivity experiments about collapse area, the amplitude of depression wave can reach

428   approximately 2.8 cm when the collapse height is 9.0 cm with its width identical to Exp. 3.2. Although

429   the stimulated wave strength is slightly greater than the results from Bourgault and Kelley (2004) due to

430   the different wave generation methods, it is predictable that the breaking of the larger-amplitude ISW

431   will be more dramatic with a prominent performance for model verification.
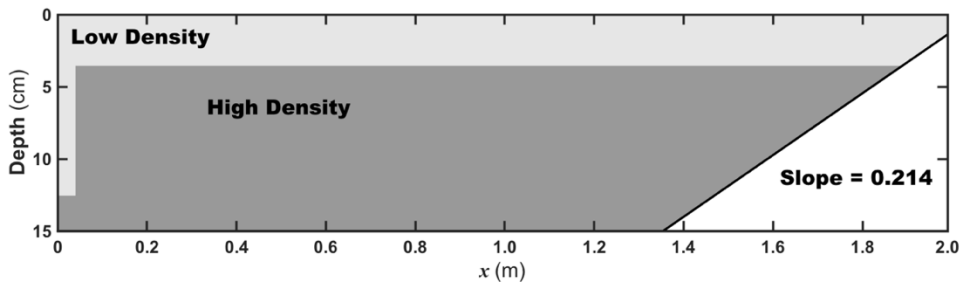
432

433   Figure 13. As in Figure 4, the low and high density are set to 1000.01 kg m^{-3} and 1047.00 kg m^{-3} with a

434   linear slope terrain placed in the east of the tank, and related configuration is referred by Bourgault and

435   Kelley (2004)

436   The associated density and velocity fields produced by the depression ISW are presented in Fig. 14

437   at t = 15 s before wave shoaling. The horizontal velocity is about 3.0 cm s⁻¹ at the surface and varies up

438   to 3.5 cm s⁻¹ at the wave core. Meanwhile, the vertical velocity distribution presents a double-core

439   structure reaching ±0.8 cm s⁻¹. The unique anticyclonic velocity characteristic just like an eastward

440   rolling wheel is consistent with the model results of Bourgault and Kelley (2004). We select the four

441   moments of the evolution of wave shoaling illustrated in Fig. 15. In addition to wave breaking

442   accompanied by the waveform steepening in the rear, a significant density fronts rolling in the wave front

443   evolves along the linear slope during the overall shoaling process in Figs. 15a and 15b. Specifically,

444   while the depression wave continues getting closer to the shallow zone, the effect of bottom friction can

445   maintain the vertical shear and increase the potential energy, which intensifies the diapycnal mixing and

446   dissipation on the density interface. Then the wave-induced diapycnal flow contributes to high-density

447   water under the interface transported continuously to the shallow zone in Fig. 15c. On the other hand,

448   there is another pronounced peculiarity in Fig. 15d compared to the Exp. 3.2. A few small-scale eddies

449   emerge along with the sheared interface due to the shear instability.
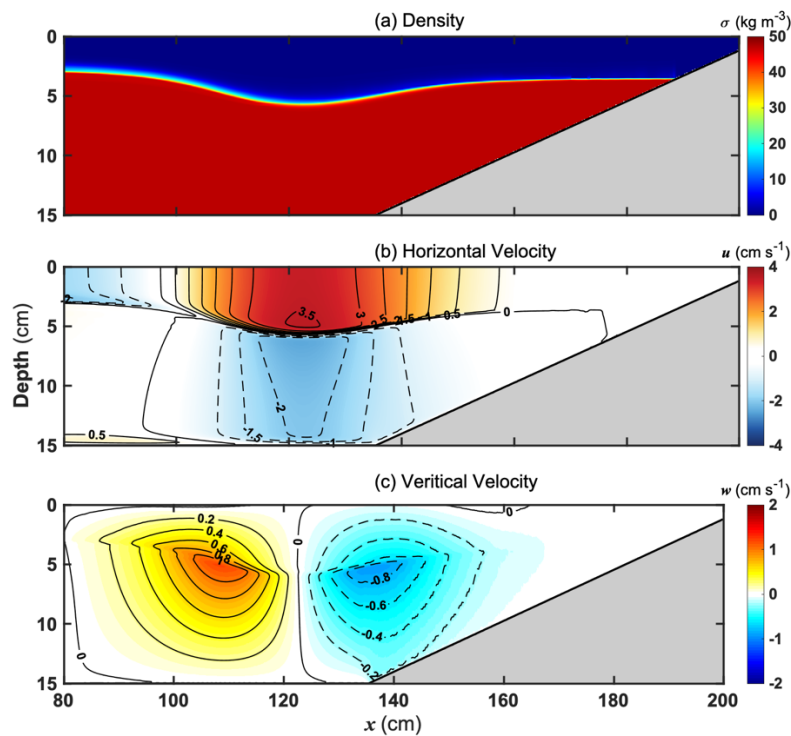
450

451   Figure 14. As in Figure 6, but with the time referring to t = 15 s before the wave shoaling.
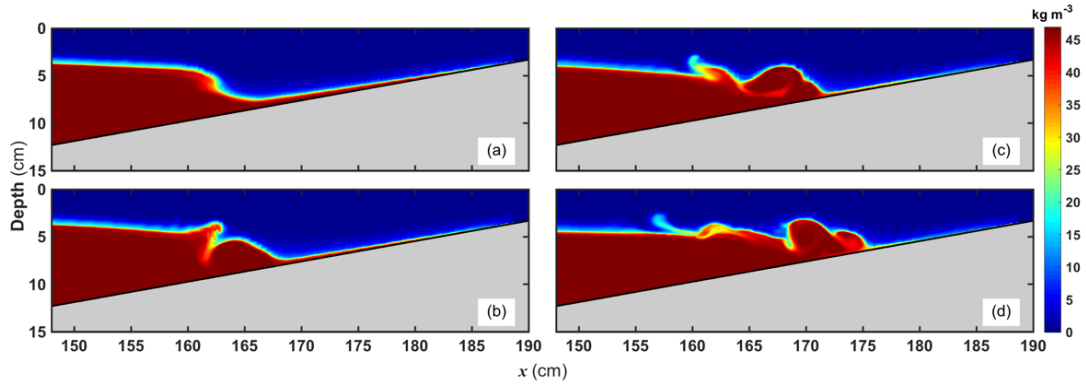
452

453   Figure 15. Wave breaking with density front rolling at t = (a) 22, (b) 23, (c) 24, and (d) 25 s.

454   To further evaluate and validate the wave breaking process, we compare the velocity field

455   distributions with the observation results via PIV technology from Michallet and Ivey (1999) and

456   nonhydrostatic numerical experiments from Bourgault and Kelley (2004) in Fig. 16. Accordingly, when

457   the depression wave arrives over the slope, its depression waveform and anticyclonic flow field are

458   modulated by the topographic shoaling to flatten the wave front and enhance the downward current along

459   the slope due to the bottom friction. Meanwhile, a smaller cyclonic eddy appears and clings to the slope

460   under the steepened wave rear in Fig. 16a. As the deformed depression wave persists in shoaling, the

461   cyclonic eddy reinforces and extends its scope of influence, resulting in a strong overturning from near

462   the bottom layer to promote the wave steepening in Fig. 16b, which presents a good agreement with the

463   results from Exp. 3.3. Afterward, the anticyclonic flow structure has been ruined since the bottom friction

464   commences hindering the current down the slope. In contrast, the coverage of the cyclonic eddy continues

465   to expand and moves the shallow zone with the waveform distorted furtherly. All the above nonlinear

466   processes are similar to the previous laboratory and model results. Our nonhydrostatic model can also

467   resolve the nonlinear evolution of the internal solitary waves at shelf break with enough high accuracy.

468
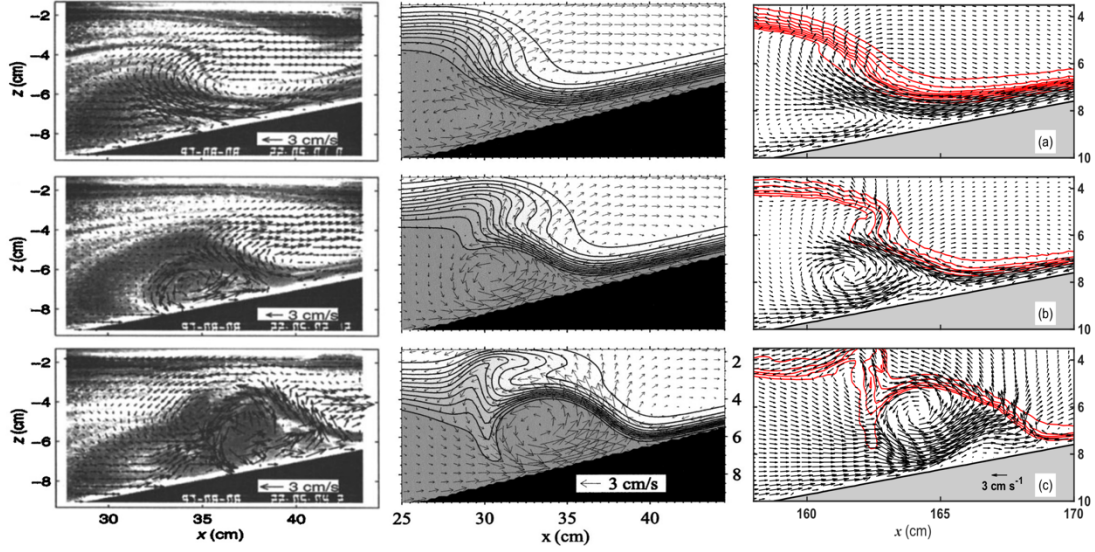
469

470   Figure 16. Comparison of velocity fields during the wave breaking on a linear slope between (left) the

471   PIV observations in the laboratory (Michallet and Ivey, 1999), (middle) the numerical model simulation

472   (Bourgault and Kelley, 2004), and (right) ORCTM simulation at t = (a) 21.7, (b) 22.2, and (c) 23.2 s

473   from top to bottom. The red contours indicate the isopycnic lines.

474 **3.5. Nonlinear Internal Waves in a double-ridge system**

475   The last validation experiment is to examine the generated nonlinear internal waves via tidal flow

476 over the varying topography. We set up an underwater double-ridge system comparable to the Luzon

477 Strait in the northern South China Sea (SCS), where the largest internal solitary waves in the world can

478 exist (Huang et al., 2016). This validation case is a 2-D problem for the reduction of computational

479 resources as well. The topography in this double-ridge system is fitted approximately with the Gaussian

480 function given as

$$H(x) = 3000 - h_w \times exp\left(-\left(\frac{x-x_w}{20 \times 10^3}\right)^2\right) - h_e \times exp\left(-\left(\frac{x-x_e}{20 \times 10^3}\right)^2\right) \quad (32)$$

481   In Eq. (32), $H(x)$ is the water depth; the height of the East and West Ridge (h_e and h_w) is 2500

482 and 1300 m in sequence with an interval and widths of 100 km, which is similar to the fundamental

483 topographic characteristics in the Luzon Strait. As shown in Fig. 17a, the static water height is 3000 m;

484 the East and West Ridge (hereafter ER and WR) are located at the coordinate origin and x = -100 km;

485 the horizontal and vertical grid resolutions are uniformly 200 m and 10 m throughout; A_{V0} and D_{V0} in

486 formulas (11) and (12) are set to 2×10^{-4} m^2 s^{-1} and 2×10^{-5} m^2 s^{-1}; the bottom friction coefficients both are

487 value of 3×10^{-3}. As for the tidal categories, the generation of semidiurnal ITs and the modulation effect

488 of diurnal ITs in the Luzon Strait determine the evolution of the larger-amplitude ISW packet in the

489 northern South China Sea (Buijsman et al., 2010a; Zeng et al., 2019), so we define the M_2 and K_1 tidal

490 currents amplitudes as 5.0 and 4.0 cm s^{-1} corresponding to the semidiurnal and diurnal components at the

491 open boundaries; the sponge thicknesses L_{sp} of the west and east boundaries are both approximately 40

492 km and the time-scale coefficient τ is set to 500 s. These model configuration in the validation experiment

493 are analogous to the control test from Li (2010) and Zhang et al. (2011) to reproduce the major structures

494 of NIWs in the South China Sea. Besides, to simplify the background environment, we also use

495 horizontally uniform stratification as the initial field for our model. Here, the reprehensive stratification

496 in Figs. 17b to 17d stems from GLORYS12V1 reanalysis product in CMEMS (Copernicus Marine

497 Environment Monitoring Service). The initial field is based on the spatial mean around the source of

498 generated ISWs in the Luzon Strait during the summer of 2011, since the large-amplitude ISWs are

499 observed during this period on the SCS continental shelf (Ramp et al., 2019) and the strong thermocline

500 structure in summer is conducive to the formation of baroclinic tides in the Luzon Strait (Zheng et al.,

501 2007; Buijsman et al., 2010b;). Additionally, the slope criticality γ (Gilbert and Garrett, 1989; Shaw et

502 al., 2009) no less than one is usually essential with the formation of linear internal waves.

$$\gamma = \frac{dH}{dx} \Big/ \sqrt{\frac{\omega^2 - f^2}{N^2 - \omega^2}} \tag{33}$$

503 in which ω is the tidal angular frequency; N^2 is the buoyancy frequency squared; the Coriolis

504 parameter f is set to zero for the earth rotation neglected due to the 2-D environment. Around East

505 Ridge γ is always larger than unity regardless of the M_2 and K_1 tide, which means East Ridge belongs

506 to the supercritical topography. Therefore, it is predictable to generate the internal waves due to the

507 interactions with barotropic flow over the East Ridge. We run the model for 10 days from an initial static

508 field. The diagnostic module is also used to characterize the high-frequency variation with the output

509 interval of 1 min at x = -250, -350 km.

510
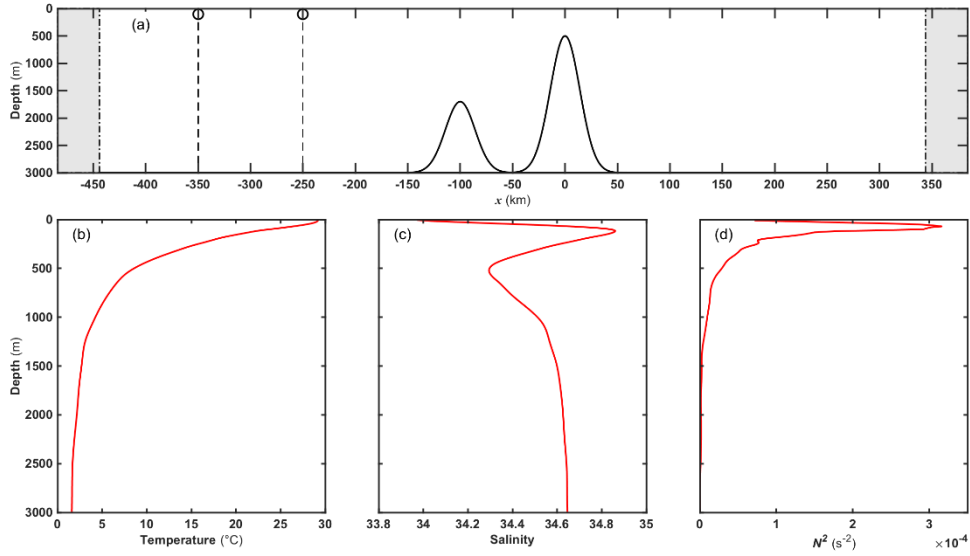
Figure 17. (a) The sketch of generated NIWs over the submerged double-ridge system case, and the

gray zones indicate the sponger layers. The summer stratification in 2011 including (b) temperature, (c)

salinity, and (d) buoyancy frequency squared are from the spatial mean within 20.25 °N–20.85 °N,

121.7 °E–122.08 °E corresponding to the source of internal waves in the Luzon Strait (Zhang et al.,

2011).

516
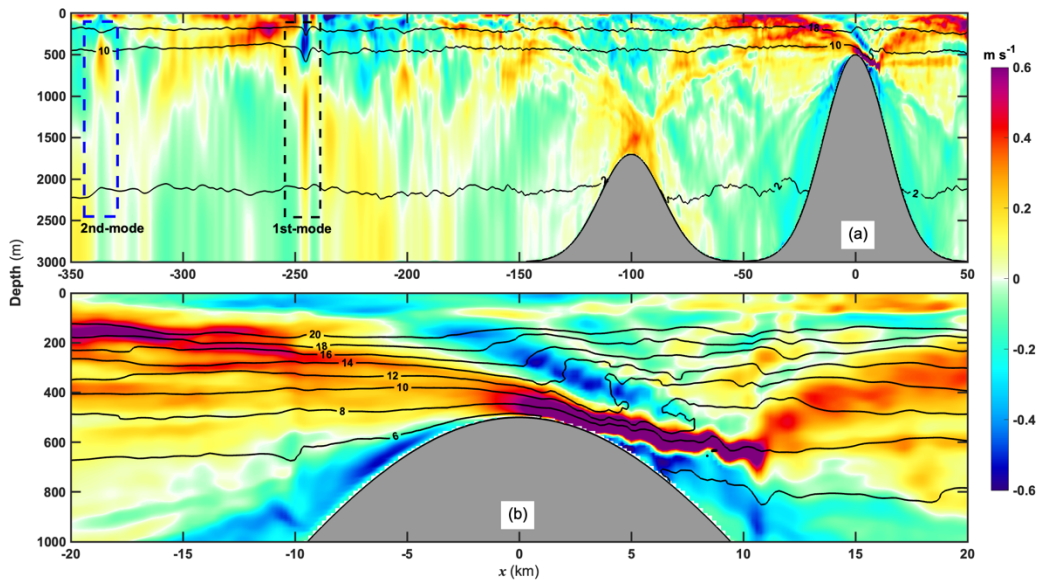
Figure 18. Distributions of horizontal baroclinic velocity with the temperature (°C) contours for

western far field (a) and source field (b) when the maximum eastward tidal current at East Ridge

reaches the end of ebb on the sixth day, where the blue (black) dashed box means the 2nd mode (1st

mode) ISW packets.

Figure 18 shows the maps of horizontal baroclinic velocity $u' = u - U$ where u is the total

velocity and U is the barotropic flow velocity. From the characteristics of the source field, it is found that the generation of internal tide beam propagating eastward and westward centered from the eastern side of East Ridge. The eastward barotropic flooding current flows continuously over the East Ridge with the maximum barotropic current up to 0.0531 m s^{-1}. A significant hydraulic jump can appear with the isotherm fluctuation up to roughly 200 m on the eastern side, which indicates the formation of Lee waves to a certain extent. Above internal waves generation due to tide-topography interactions can be described with below non-dimensional parameters at the source: (1) the tidal excursion parameter $\varepsilon = U_0/L\omega$, which can be associated with the generation of internal tide beam under the critical or supercritical topography where U_0 is barotropic current amplitude from the far field and L is the characteristic length for topography (Garret and Kunze, 2007, Chen et al., 2017). (2) the Froude number $Fr = U/c$, and its topographic form $Fr_z = \omega/N(dH/dx)$, in which c is the mode-1 linear speed for the eigenvalue problem (Legg and Adcroft, 2003; see Appendix B). Specifically, Legg and Klymak (2008) found that the nonlinear hydraulic jump will develop with lee waves generation when $Fr_z < 1/3$. It is worth noticing that the tidal excursion far less than unity agrees with the formation of the linear internal tide beam on the critical or supercritical topography but cannot ensure the formation of the Lee waves altogether. For instance, the Lee waves remain strong in the Luzon Strait despite the tidal excursion under the unity ($\varepsilon \approx 0.4$) in previous model result (Buijsman et al., 2010b). The tidal excursion parameter ε and the Froude number Fr are estimated to be 0.025 and 0.018 in Fig.18. That demonstrates that the multi-modal baroclinic tides and upstream propagation of internal waves will generate around the source field when the sub-critical barotropic current flows over the East Ridge. Furthermore, the maximum topographic Froude number is just 0.3362 around the East Ridge with the approach to the regime transition value 1/3, which ensures that the nonlinear hydraulic jump can grow with Lee waves on the east of East Ridge. All of the above can explain well the generation of the internal tide beam and hydraulic jump in our simulation and confirm to the mixed tidal lee wave regime in the Luzon Strait (Chen et al., 2017).

After the westward internal tide beam emitting from the East Ridge reaches the sea surface and reflects into the deep sea, the partial downward internal tide beam can propagate to the top of West Ridge below 1500 m depth and reflect into the upper layer again. Between the double ridges, such a more significant portion of beam energy captured by the pycnocline waveguide together with the upstream influence can strengthen the westward propagating internal waves energy in Fig. 18b, which can trace

552   back to the source of the internal solitary wave packets in the far field. However, the strong dissipation

553   for the high modal internal waves contributes to the vanishing of the internal tide beam structure and

554   allows the nonlinear evolution of low-mode baroclinic tides. The low modal internal solitary wave

555   packets can grow and propagate westward from x = -150 km, marking the disintegration of the multi-

556   modal nonlinear internal wave energy. Specifically, the first-mode ISW packet emerges from x = -250 to

557   -200 km. Meanwhile, the second-mode ISW between x = -350 and -300 km performs the convex wave

558   packet.
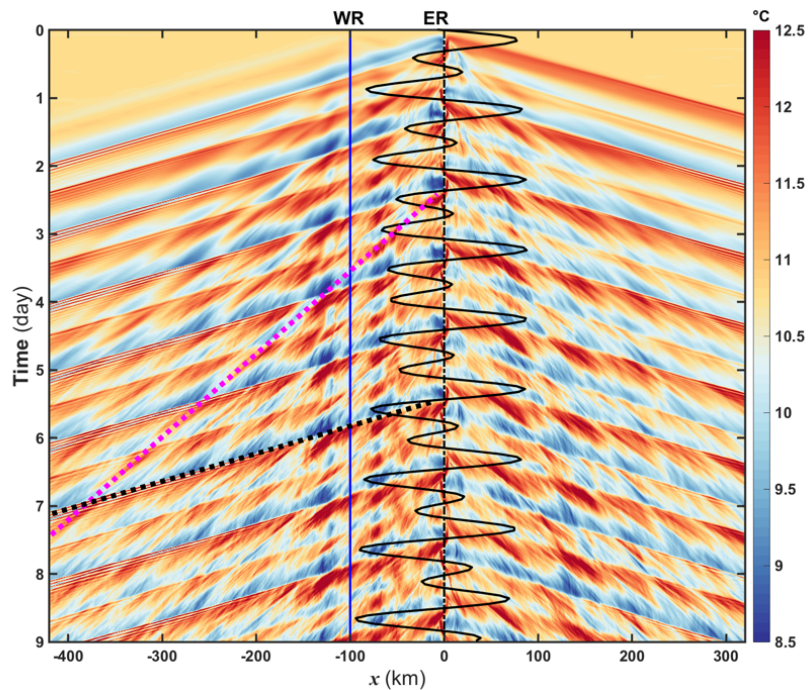
559

560   Figure 19. Hovmöller diagram about the global temperature timeseries at z = 400 m, where the time

561   interval is 15 mins. The black solid curve indicates the tidal current at the East Ridge, and the blue

562   solid line means the West Ridge location. The black and magenta dashed lines are the first and second-

563   mode internal solitary waves.

564   We can acquire the propagation characteristics of these ISWs via analyzing the global temperature

565   timeseries at 400 m depth layer. As is illustrated in Fig. 19, the second-mode ISW packet propagates

566   slower, and its strength is much weaker than the first-mode wave one. Besides, it can be distinguished

567   that the two first-mode wave packets can propagate westward in one day, one of which is stronger with

568   the structure of several tail waves, and the other is almost solitary and weak. These two types of first-

569   mode wave packets refer to the type-a and b waves (hereafter a-wave and b-wave) respectively in the

570   northern South China Sea (Ramp et al., 2004). Besides, their occurrence time can be connected to the

571 ebb of eastward flood current around East Ridge. These simulated results in the strength and timing prove

572 that a- and b-wave originate from the double-ridge in Luzon Strait (Ramp et al., 2004; 2019; Zhao and

573 Alford, 2006). Additionally, the relatively weak second-mode concave wave can be found distinctly

574 following the a-wave from the west of -300 km. To sum up, the multi-modal baroclinic tide structures

575 from the double-ridge system can propagate to the far fields. The low-mode internal waves gradually

576 perform the corresponding ISWs due to the nonlinear enhancement, which displays a good agreement

577 with the other two-dimensional experimental results (Buijsman et al., 2010a; 2010b; Vlasenko et al.,

578 2010).
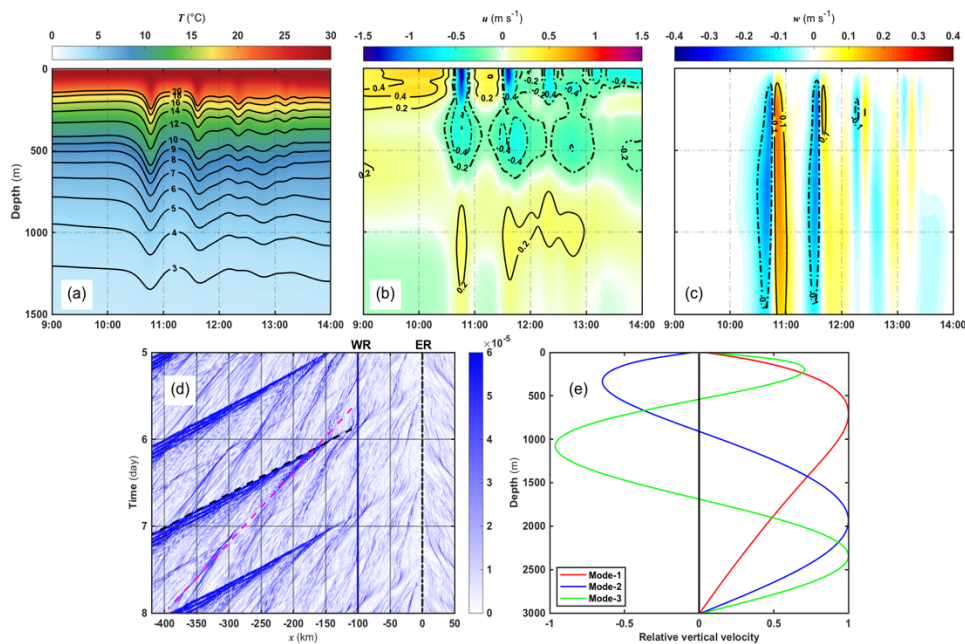
579

580 Figure 20. (a) The temperature (°C), (b) horizontal baroclinic velocity (m s⁻¹), (c), and vertical velocity

581 (m s⁻¹) structures of the first-mode ISW packet at x = -250 km on the sixth day. (d) The SSHG

582 Hovmöller diagram during the associated period where the black and magenta dashed lines indicate the

583 first and second-mode ISW packets. (e) The normal mode profiles of vertical velocity for the first three

584 modes using the Taylor-Goldstein equation.

585   To evaluate the comparison between the numerical ISWs with internal wave theory, we select the

586 results of the first-mode ISW at x = -250 km. In Fig. 20. It is found that a first-mode ISW packet

587 including three tail waves arrives at the position after 10 a.m. on the 6th day. The maximum fluctuation

588 of the first-mode ISW packet can reach 206 m located between 650 and 900 m water depths. The

589 westward horizontal baroclinic velocity associated with the wave packet prevails above 200 m with a

590 maximum strength of roughly 1.41 m s⁻¹, and the corresponding downwelling region is located between

200 and 1500 m depths with the strongest downward velocity up to 0.22 m s⁻¹. According to the Sea

Surface Height Gradient (SSHG, SSHG is defined $\sqrt{(\nabla \varsigma)^2}$) in Fig. 20d, the average propagation speed

of this wave packet is approximately 3.17 m s⁻¹ based on the slope of SSHG contour. Moreover, we solve

the Taylor-Goldstein equation (Miles, 1961; Liu, 2010; see Appendix B) 10 minutes before this wave

packet reaches x = -250 km, and the normal mode of vertical velocity is subject to the rigid-lib boundary

condition. We found that the location of the maximum modal function is 710 m in agreement with the

model results in Fig. 20e. However, the propagation speed is greater than the first-mode linear result of

2.69 m s⁻¹, which is probably attributed to the underestimated effect in linear theory. Therefore, The KdV

model is also utilized to analyze the depression wave packet. The nonlinear and dispersion parameters

are -3.4×10⁻³ s⁻¹ and 2.4×10⁵ m³ s⁻¹, which denotes that the theoretical depression wave is consistent with

the simulated results (Helfrich and Melville, 1986). Nevertheless, the theoretical nonlinear velocity of

about 2.88 m s⁻¹ is slightly lower than the simulated results. It is probable that the increasing nonlinearity

with the steepening of internal tides ultimately leads to the larger propagation speed of this first-mode

ISW packet.
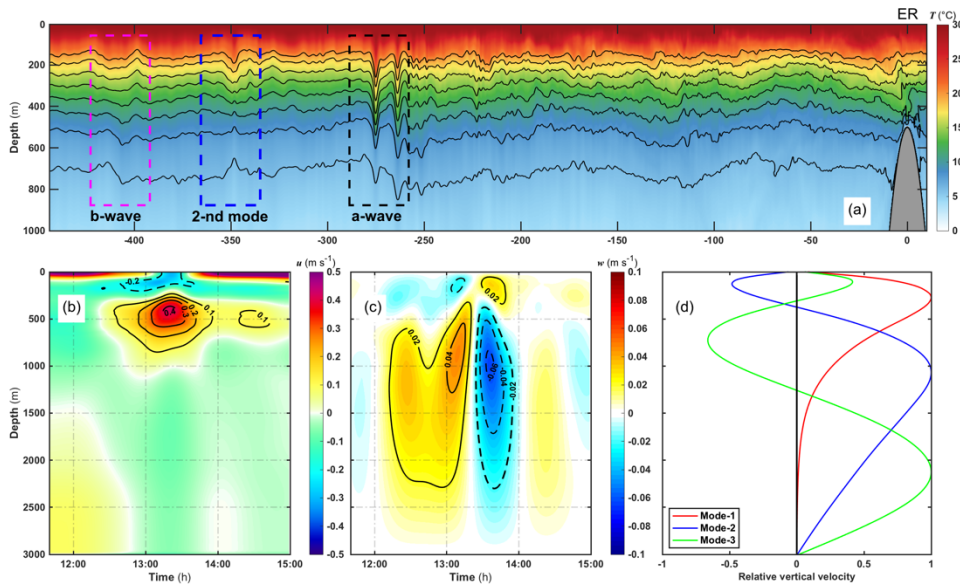
Figure 21. (a) The temperature (°C) field from the west side of East Ridge at 13:00 on the seventh day,

where dashed rectangles refer to the respective wave types. (b) The horizontal baroclinic velocity (m s⁻¹) and (c) vertical velocity (m s⁻¹) structures of the second-mode ISW at x = -350 km in the meantime.

(d) The normal mode profiles about vertical velocity for the first three modes using the Taylor-

Goldstein equation.

It is also noticeable that the multi-modal internal solitary waves field generate and get strengthen

612   gradually due to the nonlinear enhancement. In Fig. 21a, we can recognize the distinct ISW packets from

613   the isotherm displacement that refers to the type-a, second-mode, and type-b waves from the source to

614   the far field. The a-wave packet features the most substantial strength with tail waves when its vertical

615   excursion induced by the heading wave can reach up to 120 m. In contrast, the weaker b-wave contains

616   one depression soliton in the west to $x = -400$ km. They both originate from multi-modal internal tide

617   caused by the tide-topography interactions in the double-ridge system, but the b-wave is more associated

618   with the West Ridge (Buijsman et al., 2010a; Zeng et al., 2019). Between a- and b-wave, there is a second-

619   mode ISW packet classified evidently as a structure of concave wave whose upper and lower isotherm

620   fluctuate downward and upward. The maximum isotherm fluctuations are located in the roughly 180 and

621   1000 m depths and can reach up to -57.2 and 140.6 m. The propagation speed of this second-mode ISW

622   is about 1.36 m s^{-1} from the SSHG slope in Fig. 20d. It is predictable that the a-wave packet will follow

623   the second-mode signal due to the more considerable speed. Figures 21b and 21c show the second-mode

624   ISW packet and related velocity fields timeseries at $x = -350$ km. The horizontal baroclinic velocity

625   field has a sandwich-shaped vertical structure, and the maximum 0.42 m s^{-1} is located in the middle layer

626   between 200 and 600 m. The strength of baroclinic velocity with a small average of 0.2 m s^{-1} is distinct

627   from the stronger first-mode ISW packet above 200 m. Additionally, a double-peak structure performs

628   in the vertical velocity field, and it is distributed at the depths of 150 and 1000 m where the strength in

629   the deep layer is stronger than the upper, resulting in a minor isotherm fluctuation above 200 m. Here,

630   the Taylor-Goldstein equation is also solved to acquire the eigenfunction of the vertical velocity. In Fig.

631   21d, the second-mode eigenvalues have two vertical peaks whose depths correspond to 150 and 1070 m

632   with the latter strength stronger than the former, and the corresponding phase speed is about 1.34 m s^{-1}.

633   In summary, the first and second mode internal solitary waves as the leading carriers can transfer the

634   baroclinic tidal energy from the source to far fields until dissipating thoroughly. The multi-modal solitary

635   waves field conforms with the previous two-ridge experimental result using MITgcm (Vlasenko et al.,

636   2010). The internal wave theoretical models can compare well with the distribution of stimulated results

637   in our nonhydrostatic ocean model, demonstrating an overall good performance of characterizing the

638   nonlinear evolution of multi-modal baroclinic tides.

4. Discussion and Conclusion

The main focus of this paper is to introduce a newly oceanic regional nonhydrostatic circulation and tide model (ORCTM) which is rooted from the MPI-OM and aims to characterize the internal solitary wave processes of real oceans, such as in the northern South China Sea. We developed and implemented the nonhydrostatic dynamics and open boundary module under the original global hydrostatic framework of MPI-OM. Based on the fractional step and finite difference methods, ORCTM involves the three-dimensional fully nonlinear momentum equations under the Boussinesq fluid. It is needed to solve the three-dimensional Poisson equation subject to different boundary conditions before the pressure correction method is employed to acquire the velocity field corrected via nonhydrostatic pressure gradient force. In order to match the nonhydrostatic algorithm and realize larger-amplitude ISWs simulation in an ocean-scale case, an exponential relaxation term is implemented to the control equations through the sponge layers as the open boundary condition.

A series of two-dimensional ideal numerical experiments associated with the nonlinear evolution of the internal solitary waves and baroclinic tides are devised to verify this nonhydrostatic ocean model. Here, the results of the validation experiments are in accord with the theoretical framework of the nonhydrostatic dynamics and demonstrate that ORCTM can successfully characterize the generation, propagation, and dissipation of internal solitary waves in laboratory-scale cases. Specifically, the reverse situation due to wave shoaling and deepening can be depicted completely when considering the topographic change. Meanwhile, the stimulated internal solitary wave conforms with the previous numerical experiment and the direct observations in the laboratory test. Also, ORCTM can capture the density fronts with the cyclonic eddy induced by the wave breaking, which shows good stability and a high enough accuracy. Furthermore, based on the real topographic features in the Luzon Strait of the northern South China Sea, analyses of the validation experiment indicate that the multi-modal structure of baroclinic tides in the double-ridge system. The nonhydrostatic ocean model ORCTM is proven to be able to reproduce the life cycle of multi-modal ISWs induced by the tide-topography interactions in the Luzon Strait and precisely capture the alternation process of type-a and b internal solitary wave packets. The first two mode ISWs structure compares well with the internal wave theoretical model.

Even though these validation experiments have a strong resemblance to other nonhydrostatic models results (Bourgault and Kelley, 2004; Berntsen et al., 2006; Lai et al., 2010), some distinctions in

668   grid structure or numerical methods may have an opposite impact, especially when predicting a particular

669   nonhydrostatic dynamics process. Berntsen et al. (2006) indicated some noisy structures near the bottom

670   layer due to numerical errors of finite volume treatment when predicting the internal solitary wave

671   breaking via MITgcm (Marshall et al., 1997a, 1997b). They found that BOM model can avoid this

672   problem with a sigma-coordinate, whereas MITgcm needs a high-order filter to suppress the noise.

673   However, the artificial flow usually emerges and has a negative influence on the ISWs breaking

674   simulation due to the internal baroclinic pressure errors in the sigma-coordinate. Those require that model

675   users need a refined grid when encountering the area of changing topography. Compared to the

676   nonhydrostatic FVCOM (Lai et al., 2010) and BOM (Berntsen et al., 2006), ORCTM is based on the

677   finite difference method and owns a Z-coordinate, which has the capability to avoid the above errors.

678   These numerical methods and validation experiments demonstrate that ORCTM is able to approach or

679   reach an acceptable better level of the nonhydrostatic ocean model for the ISWs simulation.

680   The simulation of internal solitary waves can mirror the macroscopic structure and assist with the

681   implementation of in-situ observations. It is noticed that the predictability of nonlinear internal waves

682   characteristics relies on the model performance and external conditions such as realistic stratification,

683   bathymetry, and background circulation. Another advantage of ORCTM is the usage of the orthogonal

684   curvilinear mesh grid in the horizontal direction. It is competent enough to maintain the small-scale

685   nonhydrostatic dynamics well-resolved in the concerned region via mesh refinement. Particularly,

686   constructing the practical and reliable background fields via nested technique remains the way to move

687   forward for the ISWs simulation in the oceanic environment. Enhancing the fidelity of ISWs simulation

688   remains to be challengeable. Nevertheless, it can be concluded that our regional nonhydrostatic ocean

689   model is a good choice for oceanography scientists interested in internal waves research and numerical

690   prediction.

691

 Appendix A

693 **Discretization Algorithms of the Poisson Equation**

694   According to the idea of fractional steps (Chorin,1968; Press et al., 1988), a pressure correct method

695 on the nonhydrostatic dynamic component is employed to calculate the intermediate velocity over the

696 original hydrostatic balance scheme (Fringer et al., 2006; Lai et al., 2010). If the flow is close to the

697 hydrostatic balance, the pressure of nonhydrostatic part will be so slight that the correction plays a minor

698 role. The key to the nonhydrostatic dynamics module is to solve the Poisson equation below.

$$\frac{\partial^2 p'_{nh}}{\partial x^2} + \frac{\partial^2 p'_{nh}}{\partial y^2} + \frac{\partial^2 p'_{nh}}{\partial z^2} = \frac{\rho_c}{\Delta t} \left(\frac{\partial \tilde{u}}{\partial x} + \frac{\partial \tilde{v}}{\partial y} + \frac{\partial \widetilde{w}}{\partial z} \right) \tag{A.1}$$

699   The right-hand side (RHS) of this Eq. (A.1) is the divergence about the intermediate velocity as a

700 source or sink term. Here, based on the definition of divergence, the three components calculated directly

701 at each cell are specified in the three orthogonal coordinates as

$$\frac{\partial \tilde{u}}{\partial x} = \frac{\tilde{u}_{i,j}^k * Au_{i,j}^k - \tilde{u}_{i-1,j}^k * Au_{i-1,j}^k}{\Omega_{i,j}^k} \tag{A.2}$$

$$\frac{\partial \tilde{v}}{\partial y} = \frac{\tilde{v}_{i,j-1}^k * Av_{i,j-1}^k - \tilde{v}_{i,j}^k * Av_{i,j}^k}{\Omega_{i,j}^k} \tag{A.3}$$

$$\frac{\partial \widetilde{w}}{\partial z} = \frac{\widetilde{w}_{i,j}^k * Aw_{i,j} - \widetilde{w}_{i,j}^{k+1} * Aw_{i,j}}{\Omega_{i,j}^k} \tag{A.4}$$

702 Where i, j and k are the indices of increasing eastward, northward, and downward along x, y, and z-

703 axis, respectively; $z = 0$ is defined on the undisturbed sea surface by means of local Cartesian coordinates.

704 $\tilde{u}$, $\tilde{v}$, and $\widetilde{w}$ are the intermediate velocity; Au, Av and Aw means the six faces area of a cell in i, j

705 and k directions; Ω is the volume of a cell. These grid descriptors are defined as:

$$Au_{i,j}^k = DZw_{i,j}^k * DYu_{i,j}, \qquad Au_{i-1,j}^k = DZw_{i-1,j}^k * DYu_{i-1,j},$$

$$Av_{i,j}^k = DZw_{i,j}^k * DYv_{i,j}, \qquad Av_{i,j-1}^k = DZw_{i,j-1}^k * DXv_{i,j-1},$$

$$Aw_{i,j} = DXp_{i,j} * DYp_{i,j},$$

$$\Omega_{i,j}^k = DXp_{i,j} * DYp_{i,j} * DZw_{i,j}^k \tag{A.5}$$

706 The DX, DY and DZ represent the spacing difference between the adjacent grid cells in x, y, and z-

707 axis. The suffixes associate u, v, and w at cell face center and p' at body center. Compared to the

708 finite difference method, the definition of the divergence of a cell is more accurate and reliable especially

709 when adjacent to the solid boundaries for the RHS calculation. The left-hand side (LHS) of this equation

710 is discretized horizontally on the Arakawa C-grid (Arakawa and Lamb, 1977) using the central difference

711 method with a second-order accuracy. The vertical discretization is the same as Max Planck Institute

712   Ocean Model (Marsland et al., 2003), where the bottom grid has the capacity of the partial filled cell to

713   adjust the vertical distance for fitting into the realistic terrain (Marshall et al., 1997b). We can acquire

714   the following finite discrete equation about 7 cells for nonhydrostatic pressure perturbation as

$$
\begin{aligned}
LHS = (XW)p'^{k}_{i-1,j} + (XE)p'^{k}_{i+1,j} + (YN)p'^{k}_{i,j+1} + (YS)p'^{k}_{i,j-1} + (ZU)p'^{k-1}_{i,j} \\
+ (ZD)p'^{k+1}_{i,j} + (XC + YC + ZC)p'^{k}_{i,j}
\end{aligned}
\tag{A.6}
$$

715   where the coefficients of the discretized LHS are given as follows.

$$
XW = \frac{1}{DXu_{i-1,j} * DXp_{i,j}}, \qquad XE = \frac{1}{DXu_{i,j} * DXp_{i,j}},
$$

$$
YN = \frac{1}{DYv_{i,j-1} * DYp_{i,j}}, \qquad YS = \frac{1}{DYv_{i,j} * DYp_{i,j}},
$$

$$
ZU = \frac{1}{DZw^{k}_{i,j} * DZp^{k}_{i,j}}, \qquad ZD = \frac{1}{DZw^{k+1}_{i,j} * DZp^{k}_{i,j}},
$$

$$
XC = -\left(\frac{1}{DXu_{i-1,j}} + \frac{1}{DXu_{i,j}}\right)\frac{1}{DXp_{i,j}},
$$

$$
YC = -\left(\frac{1}{DYv_{i,j-1}} + \frac{1}{DYv_{i,j}}\right)\frac{1}{DYp_{i,j}},
$$

$$
ZC = -\left(\frac{1}{DZw^{k+1}_{i,j}} + \frac{1}{DZw^{k}_{i,j}}\right)\frac{1}{DZp^{k}_{i,j}}
\tag{A.7}
$$

716   Invoking the boundary conditions (29) and Eqs. (A.6) to (A.7), the discretized Poisson equation with 7

717   cells can be derived with the matrix form below

$$
Ap'_{nh} = B
\tag{A.8}
$$

718   Where A is a sparse, and definite-positive matrix with seven diagonals; p'_{nh} and B are the column

719   vectors with a size of all cell number $Nxyz = Nx \times Ny \times Nz$ in the model domain where Nx, Ny,

720   and Nz are the cell number in i, j and k directions. Actually, the sparse matrix A cannot easily to

721   be handled directly with a size of $Nxyz \times Nxyz$, which hence needs to be designed with greater

722   efficiency as a precondition. To apply the nonhydrostatic model to the real oceanic environment on the

723   original model base, the Portable, Extensible Toolkit for Scientific Computation (PETSc) Library is

724   implemented into the nonhydrostatic dynamic module. We apply the numerical Krylov subspace methods

725   for the matrix solvers under an MPI-based framework (Balay et al., 2020). Here, the Flexible Generalized

726   Minimal Residual (FGMRES) method (Saad, 1993) is applied to solve this problem in conjunction with

727   a multigrid preconditioner (Smith et al. 1996) for the sparse matrix before iteration. Thus, the

728   nonhydrostatic pressure can be computed with these methods. It is needed to emphasis that the

729 nonhydrostatic and hydrostatic dynamics modules remain independent of each other and not

730 contradictory. The nonhydrostatic dynamics module will make up for the deficiency of the hydrostatic

731 module only considered in this model, which means the nonhydrostatic and hydrostatic simulations can

732 be simultaneous in this model. in other words, the nonhydrostatic dynamics can be fulfilled economically

733 in harmony with the original numerical framework.

734 **Appendix B**

735 **The Korteweg–de Vries (KdV) Model in the Shallow Water**

736   Based on the shallow water approximation, a small-amplitude internal solitary wave whose

737 amplitude compared with the total depth is small enough can be described by the classical two-

738 dimensional Korteweg-de Vries (KdV) equation given as follows (Apel et al., 2007).

$$\frac{\partial \eta}{\partial t} + c\frac{\partial \eta}{\partial x} + \alpha\eta\frac{\partial \eta}{\partial x} + \beta\frac{\partial^3 \eta}{\partial x^3} = 0 \tag{B.1}$$

739   Considering two-fluid stratification system is more appropriate for the experiments in Sec. 3.1–3.3.

740 ρ_1 and ρ_2 are the upper and lower densities corresponding to the thickness h_1 and h_2; x is the

741 horizontal coordinate. Several parameters can be written here as (Benjamin, 1966; Wessels and Hutter,

742 1996)

$$\alpha = -\frac{3c}{2}\frac{\rho_1 h_2^2 - \rho_2 h_1^2}{\rho_1 h_1 h_2^2 + \rho_2 h_1^2 h_2}, \beta = \frac{c}{6}\frac{\rho_1 h_1^2 h_2 + \rho_2 h_1 h_2^2}{\rho_1 h_2 + \rho_2 h_1}, c = \sqrt{\frac{g h_1 h_2 (\rho_2 - \rho_1)}{\rho_1 h_2 + \rho_2 h_1}} \tag{B.2}$$

743 where nonlinear and dispersion parameters (α and β respectively) can represent the soliton polarity; c

744 is the linear velocity and the solution of solitary wave is expressed below the interface displacement

745 $\eta(x,t)$

$$\eta(x,t) = \eta_0 sech^2\left(\frac{x - Vt}{L}\right) \tag{B.3}$$

746 in which the η_0 is the amplitude. The nonlinear velocity V (also called phase velocity) and the

747 characteristic length of soliton L are given as.

$$V = c + \frac{\alpha}{3}\eta_0, \qquad L = \sqrt{\frac{12\beta}{\alpha\eta_0}} \tag{B.4}$$

748   The dispersion parameter β is almost larger than zero for the internal solitary waves in the ocean

749 but the sign for the nonlinear parameter α is relevant to the wave formation. When $\alpha > 0$, the interface

750 displacement will show a waveform of depression soliton. If negative, the isopycnal elevation will appear.

751 Therefore, the reverse situation for an internal solitary wave is determined by the sign change of the

752 nonlinear parameter. The KdV model is suitable with weakly nonlinear and dispersive waves which is

753 capable of being used to validate the small-amplitude ISW results in the laboratory. Nevertheless, when

754 nonlinearity enhancement happens by the reason of shallower topography or stronger stratification, the

755 modified KdV (m-KdV) model (Michallet and Barthelemy, 1998; GrimShaw et al., 2004) can describe

756 relatively stronger nonlinear solitons with the addition for cubic nonlinearity term as

$$\frac{\partial \eta}{\partial t} + (c + \alpha\eta - \alpha_1\eta^2)\frac{\partial \eta}{\partial x} + \beta\frac{\partial^3 \eta}{\partial x^3} = 0 \tag{B.5}$$

757   It is worthy of noting that the m-KdV equation takes the higher-order nonlinear term into account

758 and can degenerate into the KdV equation when the cubic nonlinear parameter $\alpha_1 = 0$. Here, the solution

759 is given with the interface displacement $\eta(x, t)$

$$\eta(x, t) = \frac{\eta_0 sech^2\left(\frac{x - Vt}{L}\right)}{1 - \mu\, tanh^2\left(\frac{x - Vt}{L}\right)} \tag{B.6}$$

760 where

$$h_c = \frac{h_1 + h_2}{1 + \sqrt{\rho_1/\rho_2}}, \qquad \bar{h} = h_2 - h_c\,,$$

$$\mu = \begin{cases} h''/h', & \bar{h} > 0 \\ h'/h'', & \bar{h} < 0 \end{cases},$$

$$h' = -\bar{h} - |\bar{h} + \eta_0|, \qquad h'' = -\bar{h} + |\bar{h} + \eta_0|\,,$$

$$V = c_{0m}\left[1 - \frac{1}{2}\left(\frac{\bar{h} + \eta_0}{h_1 + h_2 - h_c}\right)^2\right],$$

$$c_{0m} = \left\{\frac{g(h_1 + h_2)}{2}\left[1 - \left(1 - \frac{4h_c(h_1 + h_2 - h_c)(\rho_2 - \rho_1)}{\rho_2(h_1 + h_2)^2}\right)^{1/2}\right]\right\}^{1/2},$$

$$L = 2(h_1 + h_2 - h_c)\sqrt{\frac{(h_1 + h_2 - h_c)^3 + h_c^3}{3(h_1 + h_2)h'h''}} \tag{B.7}$$

761   More generally, when considering the continuously stratified fluid, the linear velocity c refers to

762 the long-wave velocity of each mode for the Strum-Liouville problem given as follows (Apel et al., 2007)

$$\begin{cases} \dfrac{d^2 W}{dz^2} + \dfrac{N^2}{c^2}W = 0 \\ W = 0, & z = 0 \\ W = 0, & z = -H \end{cases} \tag{B.8}$$

763 where H is the water depth; N is the buoyancy frequency; W is the nondimensional modal function.

764 When the nonlinear and dispersion parameters (α and β respectively) are obtained as

$$\alpha = \frac{3c \int_{-H}^{0}(dW/dz)^3 \, dz}{2 \int_{-H}^{0}(dW/dz)^2 dz}, \qquad \beta = \frac{c \int_{-H}^{0} W^2 \, dz}{2 \int_{-H}^{0}(dW/dz)^2 dz} \tag{B.9}$$

765   Besides, if still considering the background current $\overline{U}(z)$, the Taylor-Goldstein equation (Miles,

766   1961; Liu, 2010) can describe the vertical modal function W, when the nonlinear and dispersion

767   parameters are obtained under the Boussinesq approximation expressed as (GrimShaw et al., 2002).

$$\frac{d^2 \hat{\varphi}(z)}{dz^2} + \left[\frac{N^2}{(\overline{U} - c)^2} - \frac{\overline{U}''}{(\overline{U} - c)} - k^2 \right] \hat{\varphi}(z) = 0 \tag{B.10}$$

$$\alpha = \frac{3 \int_{-H}^{0}(c - \overline{U})^2 \left(\frac{dW}{dz}\right)^3 dz}{2 \int_{-H}^{0}(c - \overline{U}) \left(\frac{dW}{dz}\right)^2 dz}, \qquad \beta = \frac{\int_{-H}^{0}(c - \overline{U})^2 W^2 \, dz}{2 \int_{-H}^{0}(c - \overline{U}) \left(\frac{dW}{dz}\right)^2 dz} \tag{B.11}$$

768   where c is the n-mode linear speed; $\hat{\varphi}(z)$ is the stream function; $\overline{U}''$ are the second derivative of

769   background currents; k is the horizontal wave number.

770

Code and data availability.

The current version of the nonhydrostatic ocean model (ORCTM-v1) and these experiments about the internal solitary wave simulation in this paper are available through https://doi.org/10.5281/zenodo.6683597 (HaoHuang, 2022), as well as the experiment configurations, preprocessing, and post-processing. The PETSc library (the download address: https://petsc.org/release/download/, Balay et al., 2020) needs to be installed before building the model. Nevertheless, we also provide the PETSc library of the version in use and the ORCTM quick manual for the users at the above link.

Author contributions.

HH and PS developed the nonhydrostatic dynamic framework in ORCTM and devised the internal solitary wave validation experiments. SQ and JG developed the open boundary module. HH and SQ analyzed the model results and interpreted the concepts, and all authors contributed to the writing of the paper.

Competing interest.

The authors of this paper declare that they have no conflicts of interest.

Acknowledgements.

This study has been conducted using the E.U. Copernicus Marine Service Information global ocean. Specifically, the GLORYS12V1 product in CMEMS eddy-resolving reanalysis is extracted during the summer of 2011 whose DOI is: https://doi.org/10.48670/moi-00021.We also thank both National Supercomputing Center in Jinan and the Marine Big Data Center of Institute for Advanced Ocean Study at Ocean University of China for the provision of computing resources.

Financial support.

This research has been supported by the National Key Research and Development Program of China, Grant 2021YFF0704002 (Super-resolution assimilation and fusion model for ocean data, SAFMOD), the National Natural Science Foundation of China (NSFC), Grant No. 9195820006 (Fundamental research on stereo-sensor detection system and seismic ocean imaging of submarine), and the National Natural Science Foundation of China (NSFC), Grant No.42276011 (Study on the mechanism of generation and evolution of internal tide in the Luzon Strait influenced by background current and horizontal inhomogeneous stratification),

References

Arakawa, A., and Lamb, V. R.: Computational design of the basic dynamical processes of the UCLA general circulation model, Methods. Comput. Phys. 17, 173–265. https://doi.org/10.1016/B978-0-12-460817-7.50009-4, 1977.

Apel, J. R., Ostrovsky, L. A., Stepanyants, Y. A., and Lynch, J. F.: Internal solitons in the ocean and their effect on underwater sound, J. Acoust. Soc. Am., 121, 695-722, https://doi.org/10.1121/1.2395914, 2007.

Armfield, S. and Street, R.: An analysis and comparison of the time accuracy of fractional-step methods for the Navier–Stokes equations on staggered grids, Int. J. Numer. Meth. Fl., 38, 255-282, https://doi.org/10.1002/fld.217, 2002.

Arbic, B. K., and Scott, R. B.: On quadratic bottom drag, geostrophic turbulence, and oceanic mesoscale eddies, J. Phys. Oceanogr. 38, 84-103, https://doi.org/10.1175/2007JPO3653.1, 2008.

Ai. C., and Ding., W.: A 3D unstructured non-hydrostatic ocean model for internal waves: Ocean Dyn, 66, 1253-1270, https://doi.org/ 10.1007/s10236-016-0980-9, 2016.

Ai. C., Ma. Y., Yuan. C., and Dong, G.: Non-hydrostatic model for internal wave generations and propagations using immersed boundary method, Ocean. Eng., 225, 108801, https://doi.org/ 10.1016/j.oceaneng.2021.108801, 2021.

Benjamin, T. B.: Internal waves of finite amplitude and permanent form, J. Fluid. Mech., 25, 241-270, https://doi.org/10.1017/S0022112066001630, 1966.

Baines, P. G.: On internal tide generation models, Deep-Sea. Res., 29, 307-338, https://doi.org/10.1016/0198-0149(82)90098-X, 1982.

Bourgault, D. and Kelley, D. E.: A laterally averaged nonhydrostatic ocean model, J. Atmos. Ocean. Tech., 21, 1910-1924, https://doi.org/10.1175/JTECH-1674.1, 2004.

Berntsen, J., Xing, J., and Alendal, G.: Assessment of non-hydrostatic ocean models using laboratory scale problems, Cont. Shelf. Res., 26, 1433-1447, https://doi.org/10.1016/j.csr.2006.02.014, 2006.

Buijsman, M. C., Kanarska, Y., and McWilliams, J. C.: On the generation and evolution of nonlinear internal waves in the South China Sea, J. Geophys. Res.-Ocean, 115, C02012, https://doi.org/10.1029/2009JC005275, 2010a.

Buijsman, M. C., McWilliams, J. C., and Jackson, C. R.: East-west asymmetry in nonlinear internal waves from Luzon Strait, J. Geophys. Res.-Ocean, 115, C10057, https://doi.org/ 10.1029/2009JC006004, 2010b.

Balay, S., Abhyankar, S., Adams, Mark F., Brown, J., Brune, P., Buschelman, K., Dalcin, L., Dener, A., Eijkhout, V., Gropp, W., Karpeyev, D., Kaushik, D., Knepley, M., May, D., McInnes, L. Curfman, Mills, R., Munson, T., Rupp, K., Sanan, P., Smith, B., Zampini, S., Zhang, H., and Zhang, H.: PETSc Users Manual, Tech. Rep. ANL-95/11-Revision 3.13, Argonne National Laboratory, https://doi.org/10.2172/1614847, 2020.

Chorin, A. J.: Numerical solution of the Navier–Stokes equations, Math. Comput., 22, 745-762, https://doi.org/10.2307/2004575, 1968.

Chen, C., Liu, H., and Beardsley, R. C.: An unstructured grid, finite-volume, three-dimensional, primitive equations ocean model: application to coastal ocean and estuaries, J. Atmos. Ocean. Tech., 20, 159-186, https://doi.org/10.1175/1520-0426(2003)020<0159:AUGFVT>2.0.CO;2, 2003.

Chen, X., Jungclaus, J., Thomas, M., Maier-Reimer, E., Haak, H., and Suendermann, J.: An oceanic general circulation and tide model in orthogonal curvilinear coordinates, Amer. Geophys. Union., Fall Meeting 2005, San Francisco, CA, December 2005, Abstract OS41B-0600, 2005.

846 Chen, Z., Nie, Y., Xie, J., Xu, J., He, Y., and Cai, S.: Generation of internal solitary waves over a large
847   sill: From Knight Inlet to Luzon Strait, J. Geophys. Res.-Ocean, 122, 1555–1573.
848   https://doi.org/10.1002/2016JC012206, 2017.

849 Cushman-Roisin, B.: Kelvin–Helmholtz instability as a boundary-value problem. Environ. Fluid. Mech.,
850   5, 507-525, https://doi.org/10.1007/s10652-005-2234-0, 2005.

851 Duda, T. F., Morozov, A. K., Howe, B. M., Brown, M. G., Speer, K., Lazarevich, P., Worcester, P. F., and
852   Cornuelle, B. D.: Evaluation of a long-range joint acoustic navigation/thermometry system, Oceans-
853   IEEE., 1-6, https://doi.org/10.1109/OCEANS.2006.306999, 2006.

854 Fofanoff, P., and Millard, R. C.: Algorithms for computation of fundamental properties of seawater,
855   Unesco. R. M., 44, 203-209, https://doi.org/10.1016/j.saa.2012.12.093, 1983.

856 Fringer, O. B., Gerritsen, M., and Street, R. L.: An unstructured-grid, finite-volume, nonhydrostatic,
857   parallel coastal ocean simulator, Ocean. Model., 14, 139-173,
858   https://doi.org/10.1016/j.ocemod.2006.03.006, 2006.

859 Gilbert, D., and Garrett, C.: Implications for ocean mixing of internal wave scattering off irregular
860   topography, J. Phys. Oceanogr., 19, 1716-1729, https://doi.org/10.1175/1520-
861   0485(1989)019<1716:IFOMOI>2.0.CO;2, 1989.

862 Gerkema, T., and Zimmerman, J. T. F.: Generation of nonlinear internal tides and solitary waves, J. Phys.
863   Oceanogr., 25, 1081-1094, https://doi.org/10.1175/1520-0485(1995)0252.0.CO;2, 1995.

864 Grue, J., Jensen, A., Rusås, P. O., and Sveen, J. K.: Breaking and broadening of internal solitary waves,
865   J. Fluid. Mech., 413, 181-217, https://doi.org/10.1017/S0022112000008648, 2000.

866 GrimShaw, R., PelinovSky, E., and Poloukhina, O.: Higher-order Korteweg-de Vries models for internal
867   solitary waves in a stratified shear flow with a free surface, Nonlinear. Proc. Geoph., 9, 221-235,
868   https://doi.org/10.5194/npg-9-221-2002, 2002.

869 Grimshaw, R., Pelinovsky, E., Talipova, T., and Kurkin, A.: Simulation of the transformation of internal
870   solitary waves on oceanic shelves, Journal of physical oceanography, J. Phys. Oceanogr., 34, 2774-
871   2791, https://doi.org/10.1175/JPO2652.1, 2004.

872 Garrett, C., and Kunze, E.: Internal tide generation in the deep ocean, Annu. Rev. Fluid. Mech., 39, 57-
873   87, https://doi.org/10.1146/annurev.fluid.39.050905.110227, 2007.

874 Helfrich, K. R., and Melville, W. K.: On long nonlinear internal waves over slope-shelf topography, J.
875   Fluid. Mech., 167, 285-308, http://dx.doi.org/10.1017/S0022112086002823, 1986.

876 Härtel, C., Meiburg, E., and Necker, F.: Analysis and direct numerical simulation of the flow at a gravity-
877   current head. Part 1. Flow topology and front speed for slip and no-slip boundaries, J. Fluid. Mech.,
878   418, 189-212, http://dx.doi.org/10.1017/s0022112000001221, 2000.

879 Huang, X., Chen, Z., Zhao, W., Zhang, Z., Zhou, C., Yang, Q., and Tian, J.: An extreme internal solitary
880   wave event observed in the northern South China Sea, Sci. Rep-UK., 6, 1-10,
881   http://dx.doi.org/10.1038/srep30041, 2016.

882 HaoHuang.: HuangOCEAN02/ORCTM: ORCTM v1.1.1 (ORCTMv1.1.1), Zenodo [code],
883   https://doi.org/10.5281/zenodo.6683597, 2022.

884 Kanarska, Y., Shchepetkin, A., McWilliams, J. C.: Algorithm for non-hydrostatic dynamics in the
885   regional oceanic modeling system, Ocean. Model., 18, 143-174,
886   http://dx.doi.org/10.1016/j.ocemod.2007.04.001, 2007.

887 Ko, D. S., Martin, P. J., Rowley, C. D., and Preller, R. H.: A real-time coastal ocean prediction experiment
888   for MREA04, J. Marine. Syst., 69, 17-28, http://dx.doi.org/10.1016/j.jmarsys.2007.02.022, 2008.

889 Lawrence, G. A., Browand, F. K., and Redekopp, L. G.: The stability of a sheared density interface, Phys.

890   Fluids. A-FLUID., 3, 2360-2370, https://doi.org/10.1063/1.858175, 1991.

891   Legg, S., and Adcroft, A.: Internal wave breaking at concave and convex continental slopes, J. Phys.
892   Oceanogr., 33, 2224-2246, https://doi.org/10.1175/1520-
893   0485(2003)033<2224:IWBACA>2.0.CO;2, 2003.

894   Legg, S., and Klymak, J.: Internal hydraulic jumps and overturning generated by tidal flow over a tall
895   steep ridge, J. Phys. Oceanogr., 38, 1949-1964, https://doi.org/10.1175/2008JPO3777.1, 2008.

896   Lai, Z., Chen, C., Cowles, G. W., and Beardsley, R. C.: A nonhydrostatic version of FVCOM: 1.
897   Validation experiments, J. Geophys. Res.-Ocean, 115, C11010,
898   https://doi.org/10.1029/2009JC005525, 2010.

899   Liu, Z.: Instability of baroclinic tidal flow in a stratified fjord, J. Phys. Oceanogr., 40, 139-154,
900   https://doi.org/10.1175/2009JPO4154.1, 2010.

901   Liu, Z., Lin, L., Xie, L., and Gao, H.: Partially implicit finite difference scheme for calculating dynamic
902   pressure in a terrain-following coordinate non-hydrostatic ocean model, Ocean. Model., 106, 44-57,
903   https://doi.org/10.1016/j.ocemod.2016.09.004, 2016.

904   Li, Q.: Numerical assessment of factors affecting nonlinear internal waves in the South China Sea, Prog.
905   Oceanogr., 121, 24-43, http://dx.doi.org/10.1016/j.pocean.2013.03.006, 2014.

906   Li, J., Zhang, Q., and Chen, T.: ISWFoam: A numerical model for internal solitary wave simulation in
907   continuously stratified fluids, Geosci. Model. Dev., 15, 105–127, https://doi.org/10.5194/gmd-15-
908   105-2022, 2022.

909   Miles, J. W.: On the stability of heterogeneous shear flows, J. Fluid. Mech., 10, 496-508,
910   https://doi.org/10.1017/S0022112061000305, 1961.

911   Mtfller, P.: On the diffusion of momentum and mass by internal gravity waves, J. Fluid. Mech., 77, 789-
912   823, https://doi.org/10.1017/S0022112076002899, 1976.

913   Marshall, J., Hill, C., Perelman, L., and Adcroft, A.: Hydrostatic, quasi-hydrostatic, and nonhydrostatic
914   ocean modeling, J. Geophys. Res.-Ocean, 102, 5733-5752, https://doi.org/10.1029/96JC02776,
915   1997a.

916   Marshall, J., Adcroft, A., Hill, C., Perelman L., and Heisey, C.: A finite-volume, incompressible Navier
917   Stokes model for studies of the ocean on parallel computers, J. Geophys. Res.-Ocean, 102, 5753-
918   5766, https://doi.org/10.1029/96JC02775, 1997b.

919   Marshall, J., Jones, H., and Hill, C.: Efficient ocean modeling using non-hydrostatic algorithms, J.
920   Marine. Syst., 18, 115-134, https://doi.org/10.1016/S0924-7963(98)00008-6, 1998.

921   Michallet, H., and Barthélemy, E.: Experimental study of interfacial solitary waves, J. Fluid. Mech., 366,
922   159-177, https://doi.org/10.1017/S002211209800127X, 1998.

923   Michallet, H., and Ivey, G. N.: Experiments on mixing due to internal solitary waves breaking on uniform
924   slopes, J. Geophys. Res.-Ocean, 104, 13467-13477, https://doi.org/10.1029/1999JC900037, 1999.

925   Marsland, S. J., Haak, H., Jungclaus, J. H., Latif, M. and Röske, F.: The Max-Planck-Institute global
926   ocean/sea ice model with orthogonal curvilinear coordinates, Ocean. Model., 5, 91-127,
927   https://doi.org/10.1016/S1463-5003(02)00015-X, 2003.

928   Ma, Q., Yuan, C., Lin, X., and Chen, X.: The investigation of internal solitary waves over a continental
929   shelf-slope, J. Oceanol. Limnol., 38, 695-706, https://doi.org/10.1007/s00343-019-9123-8, 2020.

930   Ono, H.: Algebraic solitary waves in stratified fluids, J. Phys. Soc. Jpn., 39, 1082-1091,
931   https://doi.org/10.1143/JPSJ.39.1082, 1975.

932   Osborne, A. R., Burch, T. L., and Scarlet, R. I.: The influence of internal waves on deep-water drilling,
933   J. Pet. Technol., 30, 1497-1504, https://doi.org/10.2118/6913-PA, 1978.

934   Pacanowski, R. C., and Philander, S. G. H.: Parameterization of vertical mixing in numerical models of
935   tropical oceans, J. Phys Oceanogr., 11, 1443-1451, https://doi.org/10.1175/1520-
936   0485(1981)011<1443:POVMIN>2.0.CO;2, 1981.

937   Press, W. H., Flannery, B. P., Teukolsky, S. A., and Vetterling, W. T., Numerical Recipes in C. The Art of
938   Scientific Computing, Cambridge University Press, 1988.

939   Ramp, S. R., Tang, T. Y., Duda, T. F., Lynch, J. F., Liu, A. K., Chiu, C. S., Bahr, F. L., Kim, H. R., and
940   Yang, Y. J.: Internal solitons in the northeastern South China Sea. Part I: Sources and deep water
941   propagation, IEEE. J. Oceanic. Eng., 29, 1157-1181, https://doi.org/1157-
942   1181,10.1109/JOE.2004.840839, 2004.

943   Ramp, S. R., Park, J. -H., Yang, Y. J., Bahr, F. L., and Jeon, C.: Latitudinal Structure of Solitons in the
944   South China Sea, J. Phys. Oceanogr., 49, 1747-1767, https://doi.org/10.1175/JPO-D-18-0071.1,
945   2019.

946   Saad Y.: A flexible inner-outer preconditioned GMRES algorithm, SIAM J. Sci. Comput., 14, 461-469,
947   https://doi.org/10.1137/0914028, 1993.

948   Smith, B., Bjorstad, P., and Gropp, W.: Domain Decomposition: Parallel Multilevel Methods for Elliptic
949   Partial Differential Equations. Cambridge University Press, 1996.

950   Stansby, P. K., and Zhou, J. G.: Shallow-water flow solver with non-hydrostatic pressure: 2D vertical
951   plane problems, Int. J. Numer. Meth. Fluids, 28, 541-563, https://doi.org/10.1002/(SICI)1097-
952   0363(19980915)28:33.0.CO;2-0, 1998.

953   Shchepetkin, A. F., and McWilliams, J. C.: The regional oceanic modeling system (ROMS): a split-
954   explicit, free-surface, topography-following-coordinate oceanic model, Ocean. Model., 9, 347-404,
955   https://doi.org/10.1016/j.ocemod.2004.08.002, 2005.

956   Shaw, P. T., Ko, D. S., and Chao, S. Y.: Internal solitary waves induced by flow over a ridge: With
957   applications to the northern South China Sea, J. Geophys. Res.-Ocean, 114, C02019,
958   https://doi.org/10.1029/2008JC005007, 2009.

959   Vlasenko, V., Hutter, K.: Numerical experiments on the breaking of solitary internal waves over a slope–
960   shelf topography, J. Phys. Oceannogr., 32, 1779-1793, https://doi.org/10.1175/1520-
961   0485(2002)032<1779:NEOTBO>2.0.CO;2, 2002.

962   Vlasenko, V., Stashchuk, N., and Hutter, K.: Baroclinic tides: theoretical modeling and observational
963   evidence, Cambridge University Press, 2005.

964   Vlasenko, V., Stashchuk, N., Guo, C., and Chen, X.: Multimodal structure of baroclinic tides in the South
965   China Sea, Nonlinear. Proc. Geoph., 17, 529-543, https://doi.org/10.5194/npg-17-529-2010, 2010.

966   Wessels, F., and Hutter, K.: Interaction of internal waves with a topographic sill in a two-layered fluid, J.
967   Phys. Oceanogr., 26, 5-20, https://doi.org/10.1175/1520-0485(1996)026<0005:IOIWWA>2.0.CO;2,
968   1996.

969   Wolff, J. O., Maier-Reimer, E., and Legutke, S.: The Hamburg ocean primitive equation model, Tech.
970   Rep. No. 13, German Climate Computer Center (DKRZ), Hamburg, Germany, 1997.

971   Wang,Y. H., Dai, C. F., and Chen, Y. Y.: Physical and ecological processes of internal waves on an isolated
972   reef ecosystem in the South China Sea, Geophys. Res. Lett., 34, 312-321,
973   https://doi.org/10.1029/2007GL030658, 2007.

974   Zhao, Z., and Alford, M. H.: Source and propagation of internal solitary waves in the northeastern South
975   China Sea, J. Geophys. Res.-Ocean, 111, C11012, https://doi.org/10.1029/2006JC003644, 2006.

976   Zheng, Q., Susanto, R. D., Ho, C. R., Song, Y. T., and Xu, Q.: Statistical and dynamical analyses of
977   generation mechanisms of solitary internal waves in the northern South China Sea, J. Geophys.

978   Res.-Ocean, 112, C0302, https://doi.org/10.1029/2006JC003551, 2007.

979   Zhang, Z., Fringer, O. B., and Ramp, S. R.: Three-dimensional, nonhydrostatic numerical simulation of

980   nonlinear internal wave generation and propagation in the South China Sea, J. Geophys. Res.-Ocean,

981   116, C05022, https://doi.org/10.1029/2010JC006424, 2011.

982   Zeng, Z., Chen, X., Yuan, C., Tang, S., and Chi, L.: A numerical study of generation and propagation of

983   type-a and type-b internal solitary waves in the northern South China Sea, Acta Oceanol. Sin., 38,

984   20-30, https://doi.org/10.1007/s13131-019-1495-2, 2019.